Simulations for CMIP6 with the AWI climate model AWI-CM-1-1

Tido Semmler[1] (OrcID: 0000-0002-2254-4901)
Sergey Danilov[1,2] (OrcID: 0000-0001-8098-182X)
Paul Gierz[1] (OrcID: 0000-0002-4512-087X)
Helge F. Goessling[1] (OrcID: 0000-0001-9018-1383)
Jan Hegewald[1] (OrcID: 0000-0002-3675-0968)
Claudia Hinrichs[1] (OrcID: 0000-0001-5668-9167)
Nikolay Koldunov[1] (OrcID: 0000-0002-3365-8146)
Narges Khosravi[1] (OrcID: 0000-0001-7886-0236)
Longjiang Mu[1] (OrcID: 0000-0001-5668-8025)
Thomas Rackow[1] (OrcID: 0000-0002-5468-575X)
Dmitry Sein[1] (OrcID: 0000-0002-1190-3622)
Dmitry Sidorenko[1] (OrcID: 0000-0001-8579-6068)
Qiang Wang[1] (OrcID: 0000-0002-2704-5394)
Thomas Jung[1,3] (OrcID: 0000-0002-2651-1293)

[1]Alfred Wegener Institute Helmholtz Centre for Polar and Marine Research
Am Handelshafen 12
27570 Bremerhaven
GERMANY

[2]Department of Mathematics and Logistics
Jacobs University Bremen
Bremen
GERMANY

[3]University of Bremen
Bremen
GERMANY

Key Points

AWI-CM with an unstructured mesh sea-ice ocean component participates for the first time in CMIP6

The equilibrium climate sensitivity is similar to the average of CMIP5 projections and the transient climate response slightly above average

Response patterns to anthropogenic forcing are similar to CMIP5 with more pronounced Arctic sea ice loss and more stable AMOC than average

Abstract

The Alfred Wegener Institute Climate Model (AWI-CM) participates for the first time in the Coupled Model Intercomparison Project (CMIP), CMIP6. The ocean component FESOM runs on an unstructured mesh with horizontal resolutions ranging from 8 to 80 km, which is effectively one of the highest ocean resolutions used in CMIP6; it is coupled to the Max-Planck-Institute atmospheric model ECHAM 6.3 at around 100 km horizontal resolution. AWI-CM performs better than the average of CMIP5 models when compared to observations with objective performance indices. AWI-CM shows an equilibrium climate sensitivity of 3.2°C similar to the CMIP5 average, and a transient climate response of 2.1°C which is slightly higher than the CMIP5 average of around 1.8°C. The negative trend of Arctic sea ice extent over the past 30 years is weaker in our simulations compared to observations. Patterns and even magnitude of simulated changes at the end of this century compared to present-day climate according to the strong emission scenario SSP585 are very similar to the multi-model CMIP5 mean. 11°C warming north of the Barents Sea and around 2 to 3°C over most parts of the ocean as well as Arctic, subpolar, tropical and Southern Ocean wetting are simulated. Furthermore, in the northern mid-latitudes in boreal summer and autumn as well as in the nouthern mid-latitudes throughout the year a more zonal atmospheric flow is projected. Around 2070, less than 1 Million km^2 of Arctic and Antarctic sea ice remain in September and March, respectively, in the strong emission scenario simulation.

Plain Language Summary

The Alfred Wegener Institute Helmholtz Centre for Polar and Marine Research (AWI) participates for the first time with a global climate model in an international climate model comparison. The results of this and previous model comparisons feed into the next assessment report of the Intergovernmental Panel on Climate Change (IPCC). This and previous assessment reports of the IPCC are summaries on the knowledge of climate change. The assessment reports include information on past and expected climate change for the future and are written for policy- and decision-makers as well as for the general public.

In this paper the main characteristics of the AWI climate model are described and compared to previous model simulations. The projected global warming is similar to the average of previous climate models although the Arctic sea ice extent declines faster than this average. Areas that are wet in present-day climate become wetter and areas that are dry in present-day climate become drier in the future. This is consistent to previous climate model simulations. The ocean currents remain rather stable in the AWI climate simulations which leads to a continued warm Gulf stream and therefore a rather pronounced warming of the North Atlantic and parts of Europe.

Keywords

Global climate model, AWI climate model, Coupled Model Intercomparison Project, climate change, unstructured mesh

1 Introduction

Around 50 institutions worldwide are participating in the current phase of the Coupled Model Intercomparison Project 6 (CMIP6, Eyring et al., 2016). The Alfred Wegener Institute Helmholtz Centre for Polar and Marine Research in Germany, contributes for the first time in CMIP with its own ocean model FESOM (Finite Element Ocean Sea Ice Model) coupled to the atmosphere model ECHAM6 developed at Max-Planck-Institute (MPI) for Meteorology in Hamburg. The novelty of the global ocean model FESOM is its global unstructured mesh that only few institutions worldwide are employing at this stage (e.g. Petersen et al., 2019, Korn, 2017). Through this unstructured-mesh approach it is possible to put a particular focus on dynamically active regions such as the North Atlantic Current, the Southern Ocean and the tropics while using relatively coarse resolution elsewhere. For the set of “Evaluation and Characterization of Klima” (DECK) and ScenarioMIP experiments a mesh with local refinement of up to 8 km in the North Atlantic Current and the Southern Ocean is used. Coupling the unstructured ocean model FESOM to ECHAM6, which is also used for the MPI-ESM contribution to CMIP6, offers the unique opportunity to investigate the influence of an alternative ocean model formulation on the results which will be exploited in further research.

Many models participating in CMIP3 and CMIP5 have common descent and share ideas and code with each other (Masson and Knutti 2011, Knutti et al, 2013). This leads to clustering of the results according to model "genealogy" and violates assumptions of model independence, that is used during some statistical analysis of model ensembles. The ocean part of the AWI-CM is a new unstructured mesh model. It is thus based on a different dynamical core compared to most of the models contributing to CMIP6. Although many parameterisations in FESOM are similar to conventional structured-grid ocean models, and although the ECHAM model already participated since CMIP3 in the CMIP efforts (Stevens et al., 2013), it can be argued that the addition of an unstructured-mesh ocean model is an important contribution to the diversity of the CMIP6 ensemble. Large-scale characteristics dominated by the formulation of the atmosphere, such as the equilibrium climate sensitivity, are not expected to be influenced too much by the ocean formulation. In contrast, the ocean has the potential to modulate the transient evolution and regional patterns of the response considerably, and can lead to differences in projected changes of coupled phenomena such as the El Niño-Southern Oscillation (ENSO) and sea ice.

In section 2, a very brief model description and a summary of the performed DECK and ScenarioMIP simulations in the CMIP protocol is given. Section 3 describes biases in our present-day simulations for the most important atmosphere, sea-ice, and ocean variables. The climate change signal is analyzed in detail in section 4. Discussion of the results and conclusions are given in section 5.

2 Model and simulation description

2.1 Model description

The ocean-sea ice component of AWI-CM is the Finite Element Sea Ice - Ocean Model (FESOM, see Danilov et al. (2015) for the sea ice component and Wang et al. (2014) for the ocean component). It uses unstructured meshes, that allows simulations of ocean and sea-ice dynamics with variable resolution. Such meshes also allow to refine areas of particular interest, for example better resolve narrow straits, or increase resolution in energetically active regions (Sein et al., 2016, 2017). Tools have been developed to enable the user of our data to perform analysis efficiently, see Appendix A1. Furthermore, selected variables are being published regridded to a regular latitude-longitude mesh.

The atmospheric component is the spectral atmospheric MPI model ECHAM6.3.04p1 (Stevens et al., 2013). This version of the model is also used in the MPI contribution to CMIP6, which in the future will allow intercomparison of the coupled systems that share the same atmosphere model but use different sea ice-ocean models.

A more detailed description of AWI-CM components as well as evaluation of its mean state and climate variability are provided in Sidorenko et al. (2015) and Rackow et al. (2018). AWI-CM realistically simulates many aspects of the modern climate, showing an overall performance that is generally better than the most realistic climate models participating in CMIP5. Variability patterns such as El Nino Southern Oscillation (ENSO) are realistically simulated. Shortcomings related to the North Atlantic circulation, discussed in Sidorenko et al. (2015) and Rackow et al. (2018), were solved by using K-Profile Parameterization (KPP) for vertical mixing (Large et al. 1994) in the ocean model.

2.2 Simulation description

In this paper the focus is on the DECK and ScenarioMIP simulations which are summarized in Table 1 and which are defined in the CMIP6 overview paper (Eyring et al., 2016). Before starting the 500-year coupled piControl-spinup simulation with constant pre-industrial forcing, a 10-year ocean-only simulation initialized from the EN4 ocean reanalysis (Good et al., 2013) averaged over 1950-1954 has been performed. In these 10 years of ocean-only simulation the initial adjustment of the ocean state takes place. It helps to ensure a numerically stable adjustment phase of the coupled system. The piControl simulation is a continuation of the piControl-spinup simulation. From the piControl simulation the idealized greenhouse gas forcing simulations 1pctCO2 and abrupt-4xCO2 simulations as well as the historical forcing simulations are branched off at specific years (branch-off point(s), see Table 1). At the end of the historical forcing simulations, that is at the end of the year 2014, the scenario simulations are continued with forcing prescribed from the anthropogenic forcing scenarios. These scenarios are derived from Shared Socioeconomic Pathways (SSP) (Meinshausen et al. 2019).

The idealized and historical forcing simulations have been branched off sufficiently long before the end of the piControl simulation to ensure that every year of the sensitivity simulations (idealized, historical, and scenario simulations) has a corresponding year in the piControl simulation. The climate change signal is always computed following the delta approach (e.g. Lenderink et al., 2007), that is, as the difference between the sensitivity simulation and the corresponding year(s) of the piControl simulation, to account for possible model drift.

Table 1: DECK and ScenarioMIP simulations performed with AWI-CM. The forcing of the ScenarioMIP simulations is described in more detail in Meinshausen et al. (2019).

Experiment	Experiment group	Parent experiment	Years	Branch-off point(s)	Ensemble members
Ocean-only spinup	None	None	10 years	None	1
piControl-spinup	DECK	Ocean-only spinup	500 years	After 10 years	1
piControl	DECK	piControl-spinup	500 years	After 500 years	1
1pctCO2	DECK	piControl	150 years	After 250 years	1
abrupt-4xCO2	DECK	piControl	150 years	After 250 years	1
historical	DECK	piControl	1850-2014	After 150, 175, 200, 225, 250 years	5
ssp126	ScenarioMIP	historical	2015-2100	End of 2014	1
ssp245	ScenarioMIP	historical	2015-2100	End of 2014	1
ssp370	ScenarioMIP	historical	2015-2100	End of 2014	5
ssp585	ScenarioMIP	historical	2015-2100	End of 2014	1

The ECHAM model is run at a spectral resolution of T127L95, where T127 stands for a truncation wave number 127 corresponding to about 100 km horizontal resolution in the tropics and higher horizontal (zonal) resolution towards the poles. L95 stands for 95 unequally spaced model levels with relatively high vertical resolution close to the surface and reaching up to 0.01 hPa corresponding to 80 km (i.e. high-top model version).

In our AWI-CM-1-1-MR CMIP6 contribution (Semmler et al. 2018), the FESOM model is run on a medium-resolution "MR" mesh that follows the design strategy introduced by Sein et al. (2016, 2017) (Fig. 1). The main approach is to locally increase the resolution over the areas of high sea surface height (SSH) variability observed by satellites. The "MR" mesh also has an additional focus on the North Atlantic Current region. The horizontal resolution of the mesh varies from 8 km over energetically active areas to 80 km over areas with low SSH variability. The number of surface points of the MR mesh is close to the number of points in conventional regular model grids of ¼ ° resolution. The performance of the “MR” mesh in a climate configuration with AWI-CM in comparison to several other FESOM meshes is evaluated in Rackow et al. (2019).

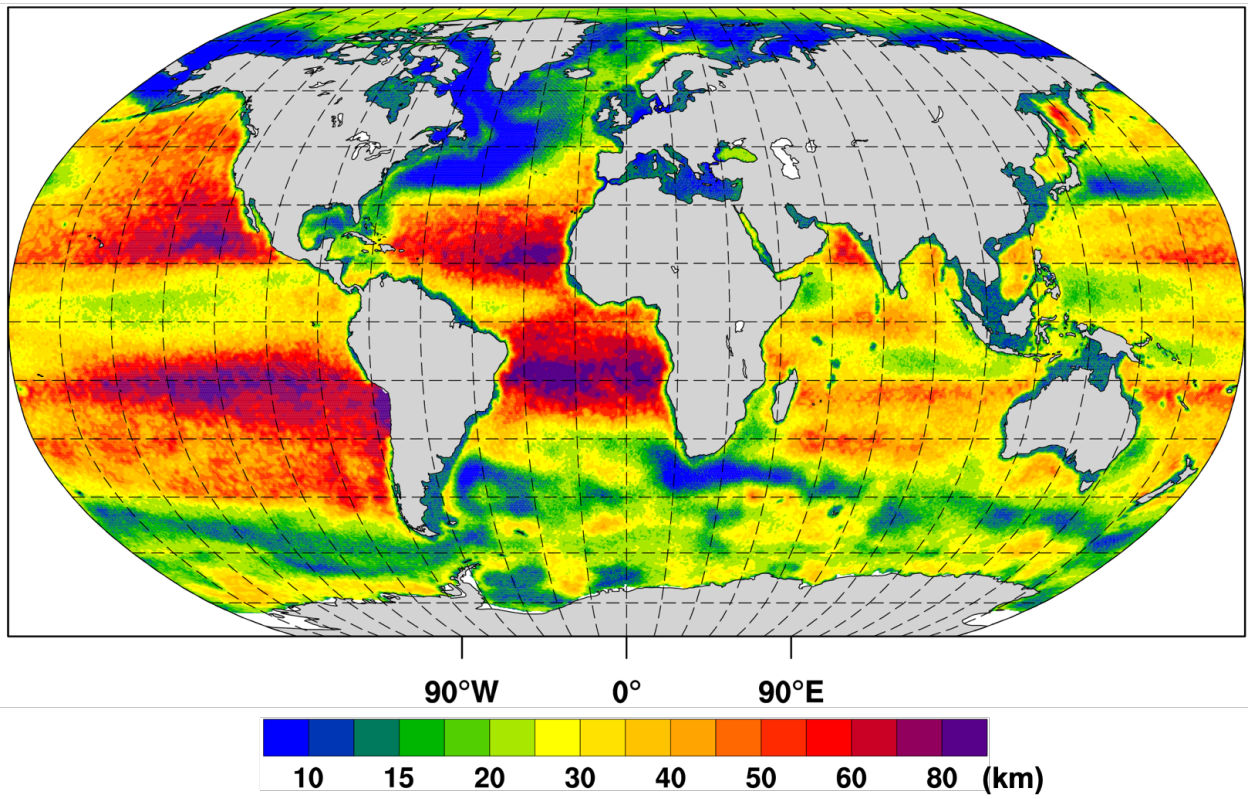

Fig. 1: FESOM MR resolution mesh applied in AWI-CM-1-1-MR for the CMIP6 DECK and ScenarioMIP simulations. Resolution is locally increased up to 8 km over eddy-active areas of high sea surface height (SSH) variability as observed by satellites (blue regions)

2.3 Cmorization and data publication

As CMIP6 is a community project, sharing our experiment result data is an important aspect. To be able to utilize data from other groups, a large set of output data has been defined where the attributes and detailed description for each dataset are put in place as a reference. These are called the CMIP6 CMOR data request (DR) tables (cmip6-cmor-tables 2019). The tables have

grown and have been clarified to a great extent over the past three years. All CMIP6 data are being published through the Earth System Grid Federation (ESGF) (Semmler et al., 2018).

From a technical point of view, we first chose which variables to generate during our model runs, as re-running the simulations is usually not feasible due to time and resource constraints. We currently produce around 150 variables matching the recent CMIP6 CMOR DR tables. The model has been optimized to be able to output the variable data in a very resource efficient manner; this enables us to use less computing resources or complete the simulations more quickly, saving energy in a corresponding amount. Due to the many changes of the requirements regarding the output contents and metadata information the CMIP6 CMOR DR tables have undergone, we had to develop a flexible strategy to transform the simulation output into the required publishable format.

As a result we now have a post processing software in place, which can directly be fed with the aforementioned DR tables to produce the output accordingly (Hegewald 2019). More details on the procedure and an explanation how to easily use unstructured mesh data from the ESGF can be found in the Appendix section A1.

3 Present-day climate from historical simulations

3.1 Performance indices

To objectively characterize the performance of the historical simulations compared to observations, we use modified performance indices by Reichler and Kim (2008) as described in Sidorenko et al. (2015) for the atmosphere and Rackow et al. (2019) for the ocean.

As reference data various observation and reanalysis data are selected: For many atmospheric variables, the ERA-40 reanalysis data are used: 2 m temperature (t2m), 10 m u wind component (u10m), 10 m v wind component (v10m), 500 hPa geopotential height (z500), and 300 hPa u component (u300). For the variables for which no observation data are assimilated into the reanalysis, the following data are used: CERES for TOA outgoing longwave radiation (toa, Loeb et al., 2012), GPCP for precipitation (pr, Huffman et al., 2009), MODIS for total cloud cover (tcc, Platnick et al., 2003), and OSISAF for sea ice concentration (sic, Tonboe et al., 2016). For the ocean, Polar Science Center Hydrographic Climatology (PHC, updated from Steele et al., 2001) is used as a reference for both potential temperature Θ and salinity S.

The absolute error is computed for each grid cell and averaged over different regions. For the atmosphere the different regions are Arctic (60-90°N), northern mid-latitudes (30-60°N), tropics (30°S-30°N), southern mid-latitudes (30-60°S), Antarctic (60-90°S), and global. For the ocean the domain is split into the major ocean basins: Arctic Ocean, North Atlantic Ocean, North Pacific Ocean, Indian Ocean, South Atlantic Ocean, South Pacific Ocean, Southern Ocean. Like for the atmosphere, the ocean is considered globally in addition. The mean absolute error is computed for each season: for the atmosphere for the four seasons DJF, MAM, JJA, SON, and for the ocean for two seasons DJF and JJA. For the ocean, model data are vertically interpolated

to the z-levels of the PHC. Errors are computed for each z-level of the climatology and averaged over the levels. Afterwards the error is normalized with the mean absolute error averaged over a set of CMIP5 models. By doing this, the performance of our new CMIP6 model can be compared objectively with the performance of CMIP5 models in terms of agreement with observation data in the historical period. A performance index of 1 means that the model performs as well as the average of the CMIP5 models. A performance index of less than 1 (more than 1) indicates a better (worse) performance.

Table 2 shows the atmosphere performance indices of the first ensemble member of historical simulations. For the other four ensemble members of historical simulations, the results are very similar. While the performance indices are first computed for each season individually, we show here the average over the seasons for brevity. Globally AWI-CM shows a good performance in all considered variables. There are few variables, precipitation and 500 hPa geopotential, which are not in all regions represented better than by the average of the CMIP5 models (only Arctic and Antarctic shown for brevity). Another weak point is the representation of Arctic sea ice concentration.

Table 2: Atmosphere performance indices for years 1985-2014 of the first ensemble member of AWI-CM historical simulations averaged over the four seasons

	t2m	u10m	v10m	toa	pr	tcc	z500	u300	sic	avg
global	0.77	0.81	0.81	0.74	0.99	0.75	0.92	0.72	-	0.81
Arctic	0.92	0.81	0.84	0.69	1.16	0.71	1.24	0.89	1.23	0.94
Antarctic	0.71	0.65	0.84	0.74	1.05	0.70	0.53	0.64	0.50	0.71

In the ocean (Table 3), potential temperature is better represented than by the average of CMIP5 models. However, this is not the case for salinity. The Pacific as well as the North Atlantic show a worse performance compared to the average of CMIP5 models. While the performance indices give a quick and objective overview of how a model performs, it is necessary to carry out further analysis to investigate if typical errors of climate models persist. Regarding the errors in potential temperature and salinity, more analysis is found in section 3.4.

Table 3: Ocean performance indices for years 1985-2014 of the first ensemble member of AWI-CM historical simulations averaged over the two seasons DJF and JJA

	Θ	S	average
global	0.79	1.15	0.97
Southern Ocean	0.96	0.70	0.83
Indian Ocean	0.69	0.94	0.82
North Pacific	0.92	1.28	1.10
South Pacific	0.81	1.14	0.98
North Atlantic	0.70	1.70	1.20
South Atlantic	0.75	0.79	0.77
Arctic Ocean	0.72	0.90	0.81

3.2 Atmospheric circulation

Figs. 2 and 3 show a too strong westerly flow above the Southern Ocean especially in austral summer (DJF). In the Euro-Atlantic sector there appears to be a southward shift of the jet stream resulting in too strong westerly flow over Southern Europe and too weak westerly flow over Northern Europe in boreal winter (DJF) and spring (MAM), a bias that has been found in CMIP5 models (Zappa et al., 2013) and that can be associated with an underestimation of Euro-Atlantic blocking (Jung et al. 2012). Especially in boreal winter, the Aleutian low is too weak as can be seen from positive biases in both the mean sea level pressure and the 500 hPa geopotential. This feature has been seen in previous ECHAM6 simulations (Stevens et al., 2013). In the Arctic region there is a positive 500 hPa geopotential height bias throughout the year which is not present in the mean sea level pressure except for boreal winter over the Barents Kara Sea region. This is indicative of a too warm Arctic atmosphere. For the tropical regions the same is valid but to a lesser extent. Biases are not negligible and amount to up to 7 hPa and 70 m in limited areas. In these areas they are comparable to the climate change signal indicating that the confidence in projections of circulation changes is low.

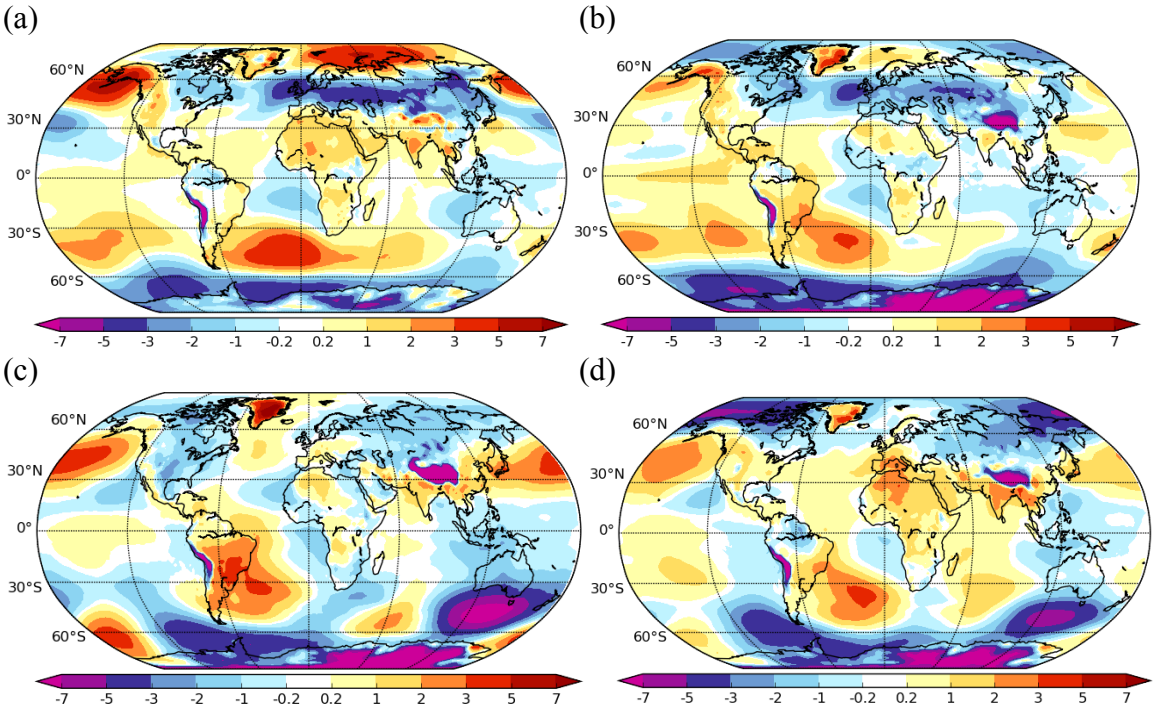

Fig. 2: Mean sea level pressure bias (hPa) as an ensemble mean over the 5 historical realizations for 1985-2014 compared to ERA40 climatology from 1957-2002. (a) DJF, (b) MAM, (c) JJA, (d) SON

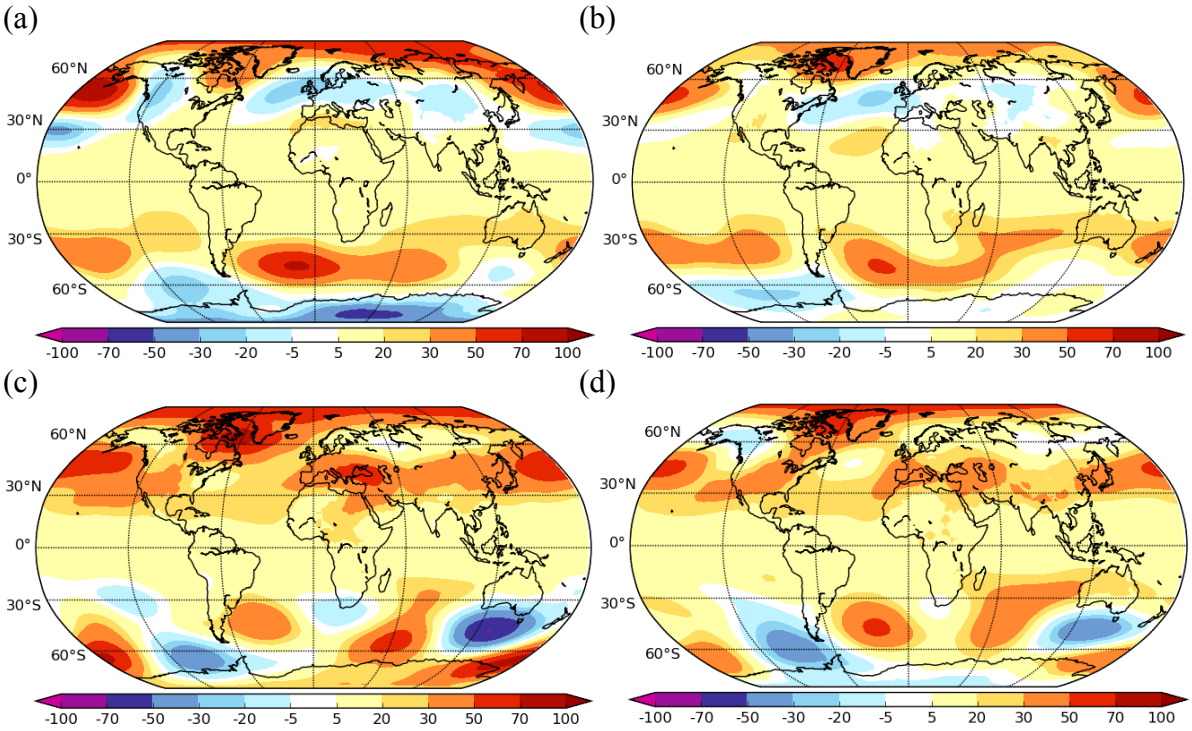

Fig. 3: 500 hPa geopotential bias (m) as an ensemble mean over the 5 historical realizations for 1985-2014 compared to ERA40 climatology. (a) DJF, (b) MAM, (c) JJA, (d) SON

3.3 ENSO statistics and phase locking

Sea surface temperature (SST) anomalies in the tropical Pacific associated with the El Niño-Southern Oscillation (ENSO) are of global concern. Since ENSO is the largest signal of interannual variability on Earth, the realistic simulation of these SST anomalies, both with respect to their absolute magnitude and temporal behaviour, is crucial for any global climate model.

When comparing area-weighted SST anomalies in the typical Niño 3.4 box (170°W-120°W, 5°S-5°N) to observations, we find that the 5 historical ensemble members with AWI-CM depict a realistic distribution (Fig. 4). To assess the temporal behaviour, we consider a slightly more advanced diagnostic, the seasonal phase locking of Niño 3.4 SST anomalies to the seasonal cycle (Fig. 5). Observed SST variability, as diagnosed from monthly standard deviation, tends to peak in boreal winter, with a minimum in spring. Especially in boreal winter, the 5 ensemble members capture the U-shape and its magnitude relatively well; however, there is a bias in spring where the simulations tend to show a second peak, which is not present in the observations. A bias of similar magnitude had already been identified in a previous configuration of AWI-CM, using the 'REF' ocean grid at 0.25° tropical resolution (Rackow and Juricke, 2019). The bias appears to be rather sensitive to the applied tropical ocean resolution since the second peak is much stronger at a coarser resolution of 1°, using the same atmospheric resolution (see Fig.6 in Rackow et al., 2014).

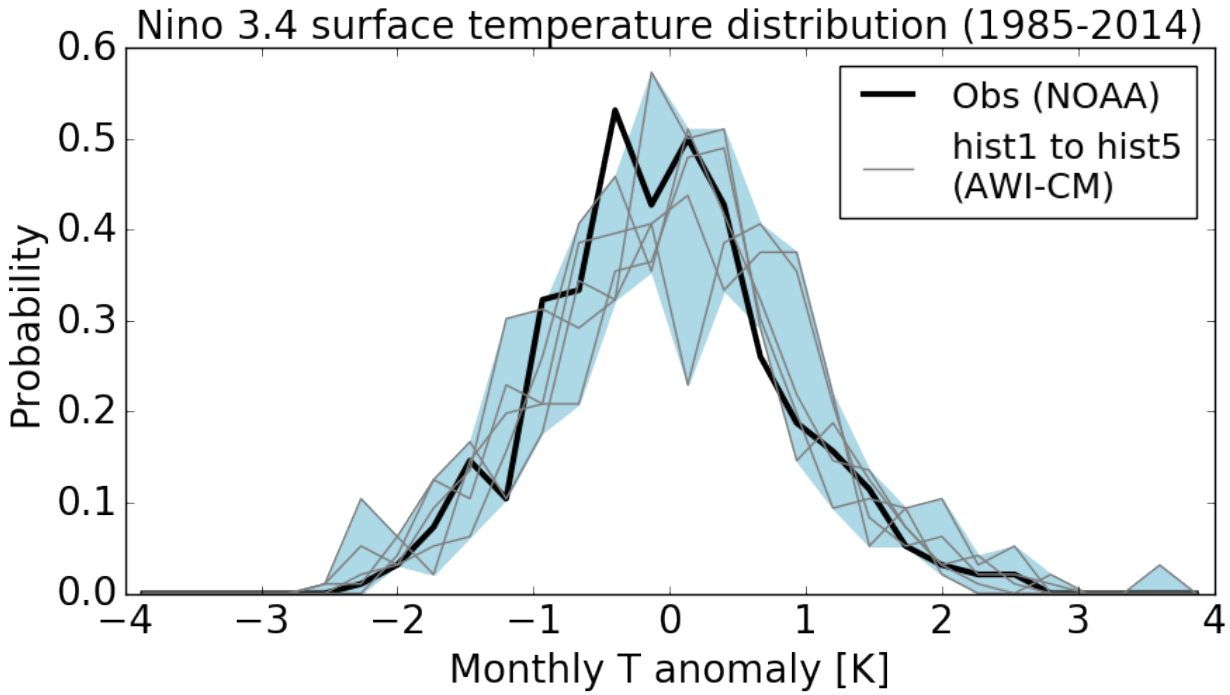

Fig. 4: Probability distribution function (PDF) of sea surface temperature anomalies in the Niño 3.4 region for the period 1985-2014. The black line gives the observed Niño3.4 PDF (1985-2014) by NOAA; individual simulated PDFs are presented with grey lines. The range of the model results is shaded in light blue.

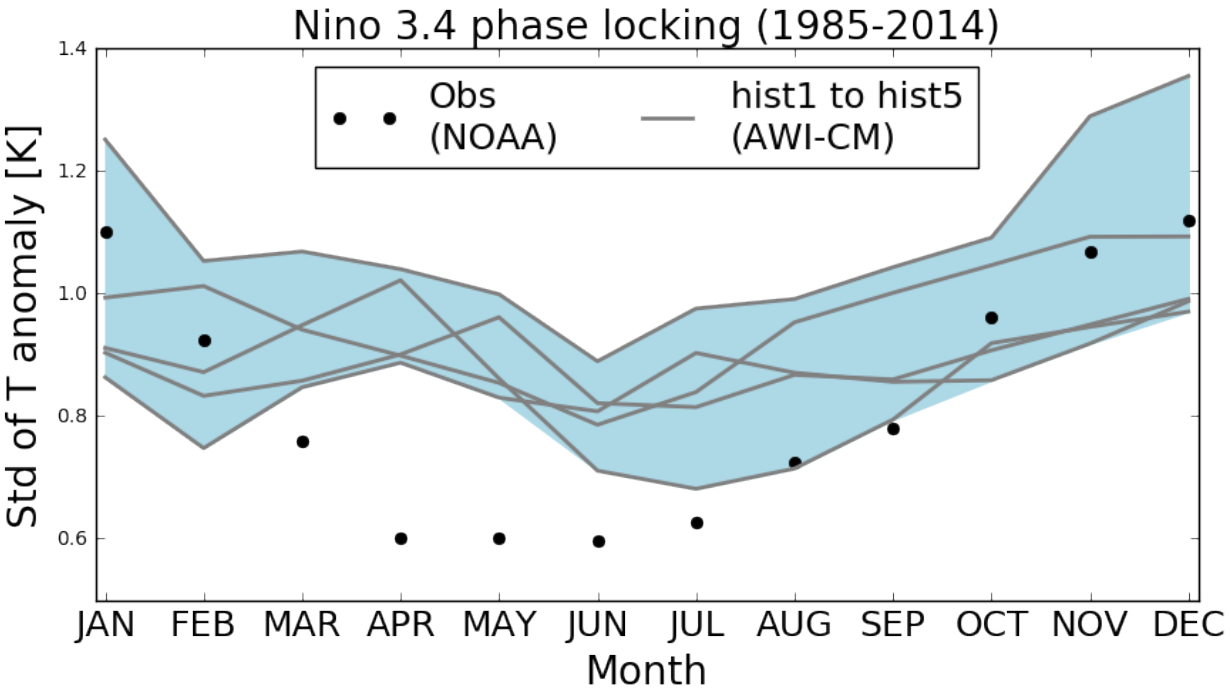

Fig. 5: Seasonal phase locking of temperature anomalies in the Niño3.4 region for 1985-2014. Black dots give the monthly standard deviation of the observed Niño3.4 index (1985-2014) by NOAA; grey lines give the standard deviations of the simulated Niño3.4 indices for the five historical ensemble members. The range of the model results is shaded in light blue.

3.4 Ocean biases

Spatial distributions of temperature and salinity biases in the interior of the ocean for historical simulations are shown in Fig 6. The potential temperature at 300 meters is too cool and the ocean is too fresh over subtropics and in general warmer and saltier over mid latitudes. There is a pronounced North Atlantic cold bias related to the too zonal pathway of the North Atlantic Current, that is present in many CMIP climate models (e.g. Wang, et al., 2014).

Warm and salty biases in the Southern Ocean are generally related to the fact that the positions of isopycnals, determined by the balance of Ekman pumping and eddy transport, are shifted. This effect on non-eddy-resolving resolutions should be parameterized (Gent and McWilliams, 1990, GM), but it usually does not work as well as explicitly resolving ocean eddies. In FESOM the GM parameterisation is gradually switched off when the resolution reaches 25 km. The horizontal resolution of the MR mesh in the Atlantic band along 40°S is finer than 25 km, so the GM parameterisation is switched off. The remaining bias might be due to the still too weak eddy activity as well as due to shift of the atmospheric front in a coupled model.

Many CMIP5 models, using coarse resolution, demonstrate a warm bias at 1000 m, which is especially strong in the Atlantic Ocean. Increase in the horizontal resolution leads to reduction of this bias, as described in Rackow et al. (2019). In the AWI-CM simulations discussed in this paper, the magnitude of the warm bias in the South Atlantic is similar to the one over most of the Pacific Ocean. The cold and fresh bias in the North Atlantic is related to the outflow and spreading of Mediteranian waters from the Strait of Gibraltar. The reasons for this bias and possible ways to reduce it are discussed in Rackow et al. (2019). The positive temperature and salinity biases in the Indian Ocean are most probably related to excessive supply of warm and salty water from the Red sea.

As was already mentioned in section 3.1, the biases in temperature and salinity compensate each other in terms of density.

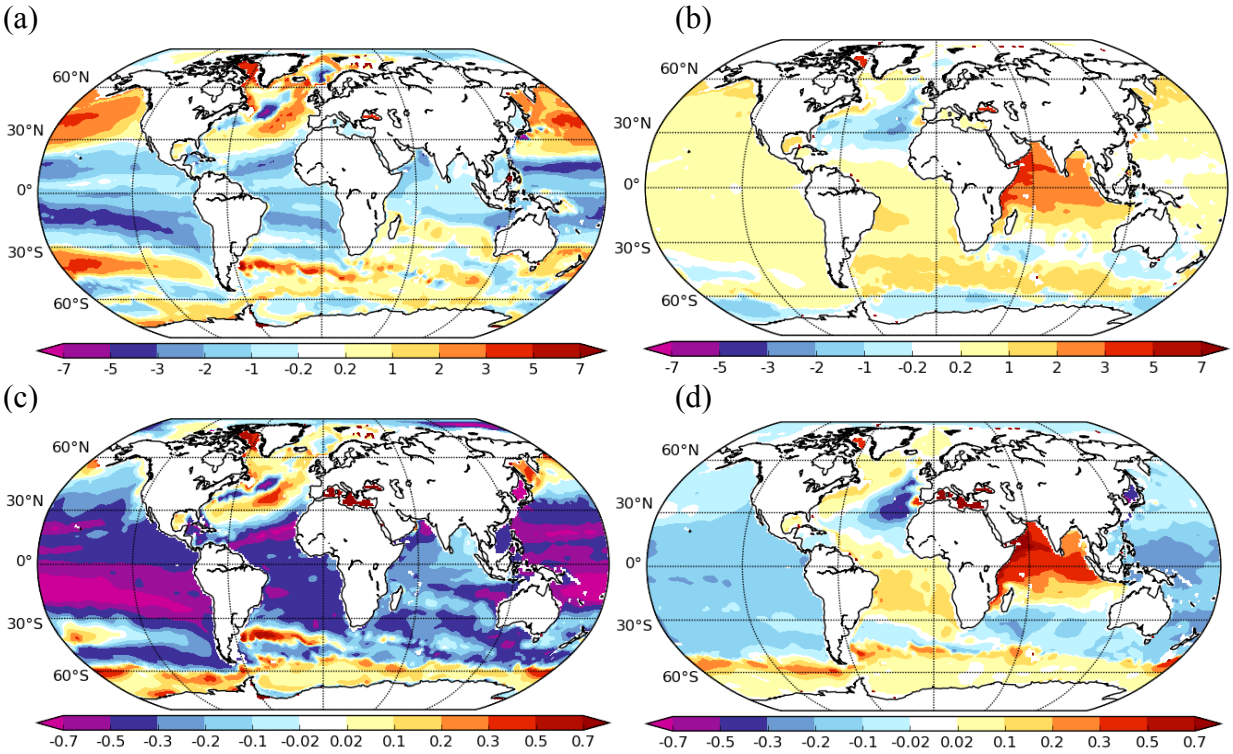

Fig. 6: Bias of the annual mean potential temperature (°C) in (a) 300 m, (b) 1000 m depth averaged over DJF 1985-2014 of hist1 simulation compared to the Polar Science Center Hydrographic Climatology (PHC, updated from Steele et al., 2001). (c) and (d) as (a) and (b) but for salinity (psu).

Below around 500 m depth into the ocean, the mean absolute error of the potential temperature is smaller in AWI-CM than in most of the CMIP5 models (Fig. 7a) while for the salinity AWI-CM is in the bulk of the CMIP5 models (Fig. 7c). When focusing on the North Atlantic Ocean potential temperature (Figs. 7b) for which various models show a pronounced warm bias in 1000 to 2000 m (Rackow et al., 2019), AWI-CM performs well. However, for salinity, in the North Atlantic (Fig. 7d) and also in the Pacific (not shown) the mean absolute error is large compared to most of the CMIP5 models.

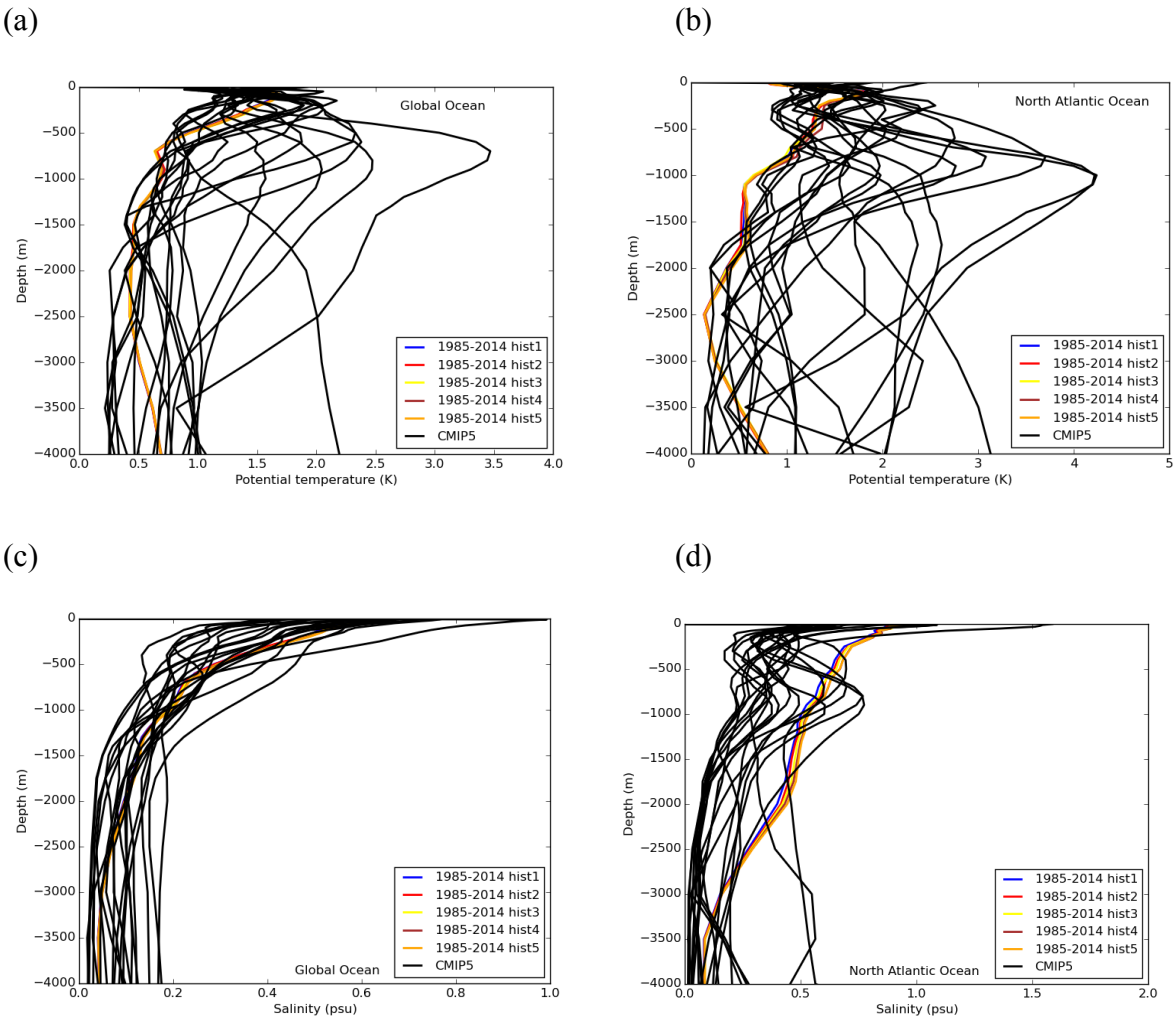

Fig. 7: Profiles of mean absolute error calculated from each grid point of the (a) globe and (b) North Atlantic ocean of potential temperature (°C) for DJF 1985-2014 of the five ensemble members of the historical AWI-CM simulation (in colors) and for DJF 1976-2005 of CMIP5 simulations (in black, each line representing one CMIP5 model). (c) and (d) as (a) and (b) but for salinity (psu). The reference climatology is the Polar Science Center Hydrographic Climatology (PHC, updated from Steele et al., 2001).

4 Climate response

4.1 Climate sensitivity

The equilibrium climate sensitivity (ECS), inferred from linear regression of the Top-of-Atmosphere (TOA) imbalance against the temperature response in the 4xCO2 simulation (Fig. 8), amounts to 3.2°C (half of the 4xCO2 equilibrium temperature difference). This is similar to the average over the CMIP5 models (IPCC, 2014). The transient climate response (TCR), computed as average response over the 30 years around year 70 from the 1pctCO2 simulation,

amounts to 2.1°C, which is slightly stronger than the average over the CMIP5 models (1.8°C, IPCC, 2014). Note that, by considering *changes* in the TOA flux and the global-mean near-surface temperature (delta approach), our estimates for the ECS and the TCR are not affected by the imbalances reported in the appendix section A2 (apart from possible non-linear effects).

Changes in the energy budget and the role of shortwave feedbacks in the historical and scenarios simulations are detailed in Sect. 4.5.

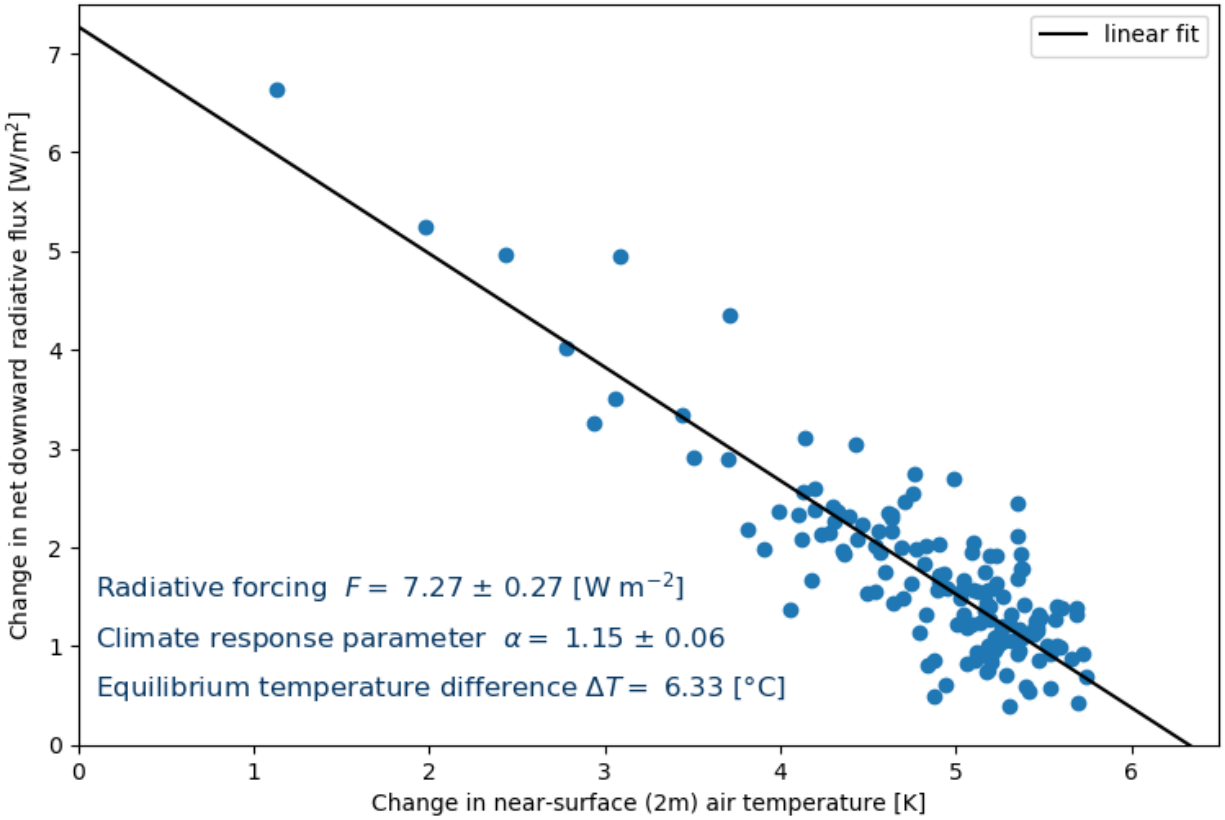

Fig. 8: Gregory plot (Gregory et al., 2004) from the abrupt-4xCO2 compared to the piControl simulation.

4.2 Surface response

4.2.1 2 m temperature and precipitation

Fig. 9 shows the development of the temperature 2 m above the surface according to the piControl, historical, and scenario simulations as global and hemispheric means. Except for interannual variability, the piControl simulation shows no trend in temperature as expected. When considering the anthropogenic forcing, the historical simulations show a warming of 1.11°C while in the observations the warming amounts to 0.86°C in 2005-2014 compared to 1891-1900. Both in the observations and in the historical simulations the Northern Hemisphere

warming is 0.2°C higher than the global average and the Southern Hemisphere warming 0.2°C lower.

Until the end of this century, the global mean temperature rises by approximately 4°C in addition to the increase up to today under the strongest emission scenario SSP585. Over the Northern Hemisphere this warming is more pronounced and amounts to approximately 5°C and over the Southern Hemisphere the warming is restricted to approximately 3°C. For the weakest scenario SSP126, the global mean warming is limited to around 1°C compared to present-day and remains just below 2°C compared to pre-industrial conditions. The SSP126 scenario has been designed to keep the global warming below 2°C - a condition that seems to be fulfilled according to our simulations. The more pronounced warming over the Northern Hemisphere compared to the Southern Hemisphere is partly due to the higher land partition in the Northern Hemisphere compared to the Southern Hemisphere. The temperature increase for both the strongest and the weakest emission scenario agrees with the CMIP5 multi-model ensemble mean (IPCC, 2014, their Figure SPM.6a).

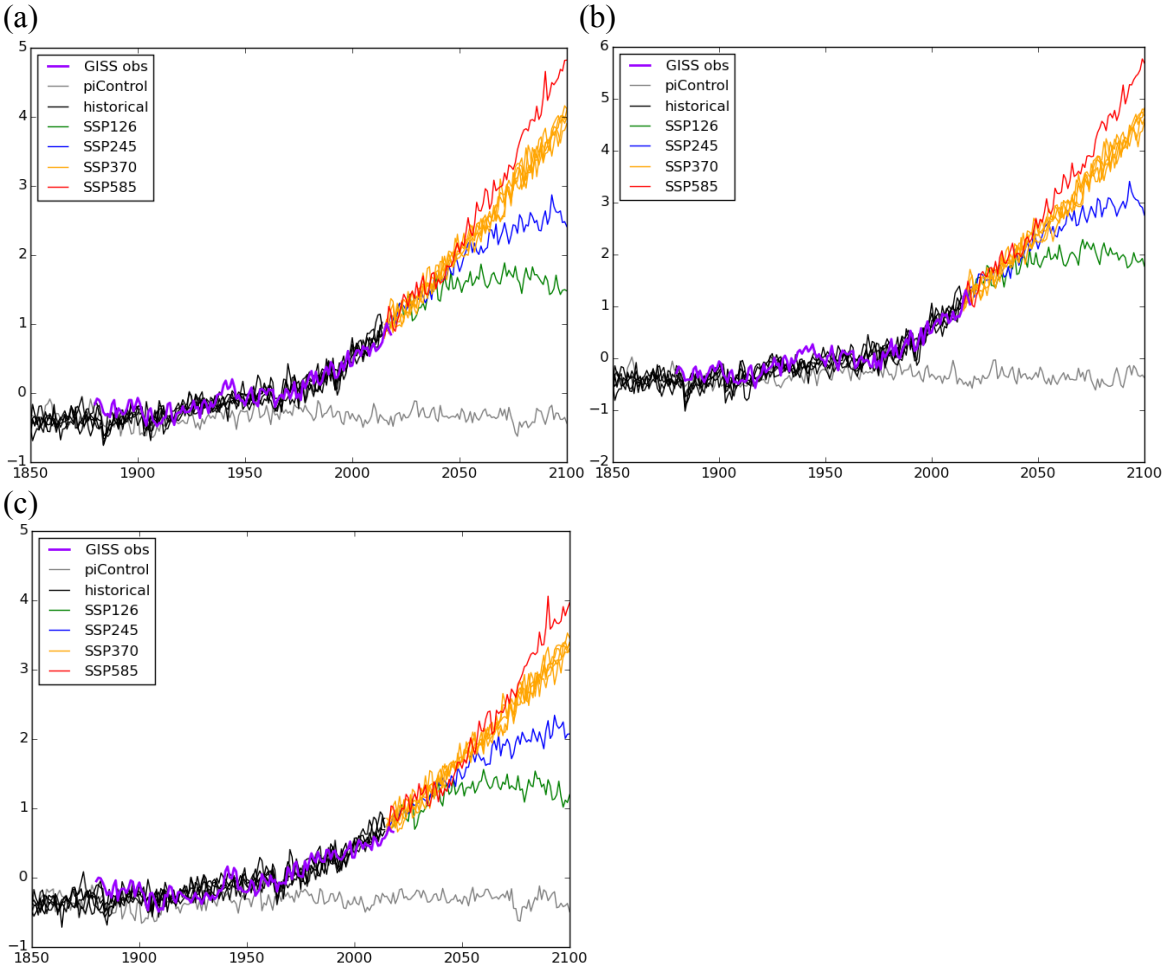

Fig. 9: (a) Global, (b) Northern Hemisphere, and (c) Southern Hemisphere mean 2 m temperature anomaly versus 1951-1980 average (°C) from piControl, historical, and scenario simulations. The purple line indicates the observed 2 m temperature anomaly from Goddard

Institute for Space Studies (GISS) Surface Temperature Analysis (GISTEMP v4) (GISS, 2019; Hansen et al., 2010; Lenssen et al., 2019).

Fig. 10 shows the spatial distribution of simulated temperature and precipitation changes until the end of the century according to the strongest emission scenario SSP585. Temperature changes are very robust and exceed the 2 standard deviations of interannual variability of the control simulation over the whole globe (Fig. 10a). Precipitation changes are clearly less robust (Fig. 10b). Large robust areas of precipitation increase include the Arctic and the Southern Ocean as well as the African tropics.

The well-known feature of Arctic Amplification and to some extent also Antarctic Amplification can clearly be seen from Fig. 10a. According to the SSP585 scenario, the temperature increases as much as 11°C around Iceland and over the Northern Barents Sea. In the northernmost parts of the European and American continents the warming exceeds 7°C at the end of the century compared to the historical reference period. Large continental areas are affected by temperature increases of more than 5°C. Also over the Weddell Sea and over parts of Antarctic temperature increases of more than 5°C are simulated. Over the ocean, the warming generally amounts to 2 to 3°C.

Over large areas of central Africa and over the tropical Pacific, precipitation increases of more than 50% are simulated. Other, more limited areas with such precipitation increases are an area west of South Africa as well as north of Greenland. Over the whole Arctic a substantial precipitation increase of more than 40% is simulated and over the Southern Ocean adjacent to the Antarctic continent extended areas are affected by precipitation increases of 20 to 30%. These described precipitation changes are very robust since they exceed twice the interannual standard deviation of the control simulation. Except for parts of the Amazonas region, simulated precipitation decreases are less robust and are mainly concentrated in subtropical areas. They do not exceed 50%.

Compared to the multi-model CMIP5 ensemble (IPCC, 2014, Summary for Policymakers, their Fig. SPM.8), the temperature response looks very similar, both regarding magnitude (11°C over Northern Barents Sea, more than 5°C over large continental areas as well as Weddell Sea and parts of Antarctica, 2 to 3°C over large parts of the ocean) and pattern of response.

The precipitation increase over the Arctic is less pronounced and the precipitation increase over Africa clearly more pronounced compared to the multi-model CMIP5 ensemble (IPCC, 2014, Summary for Policymakers, their Fig. SPM8). Otherwise, the precipitation response pattern is quite consistent.

It can be concluded that especially the temperature response pattern with strong Arctic and continental as well as weak ocean warming agrees very well with the multi-model ensemble mean of CMIP5 simulations, even in terms of magnitude. Also the feature of wetting polar, subpolar and tropical regions as well as drying subtropical regions agrees with patterns from the multi-model ensemble of CMIP5 simulations although the magnitude of the response is not as consistent as the magnitude of the temperature response.

Independent of the magnitude of the forcing (SSP126, SSP245, SSP370, SSP585), the Arctic Amplification Index computed as the warming averaged over 70 to 90°N divided by the warming globally averaged, is around 2.7 in present-day climate and gradually decreases to around 2.5 at the end of the century (not shown). There is also considerable variability with maximum and minimum values of 0.5 above and below the mean value in a five-year running mean, respectively.

The Antarctic Amplification index computed as the warming averaged over 70 to 90°S divided by the warming globally averaged, is around 1.3 during the whole remaining century, again independent of the forcing scenario. There are maximum and minimum values of 0.4 above and 0.4 below the mean value in a five-year running mean.

(a)

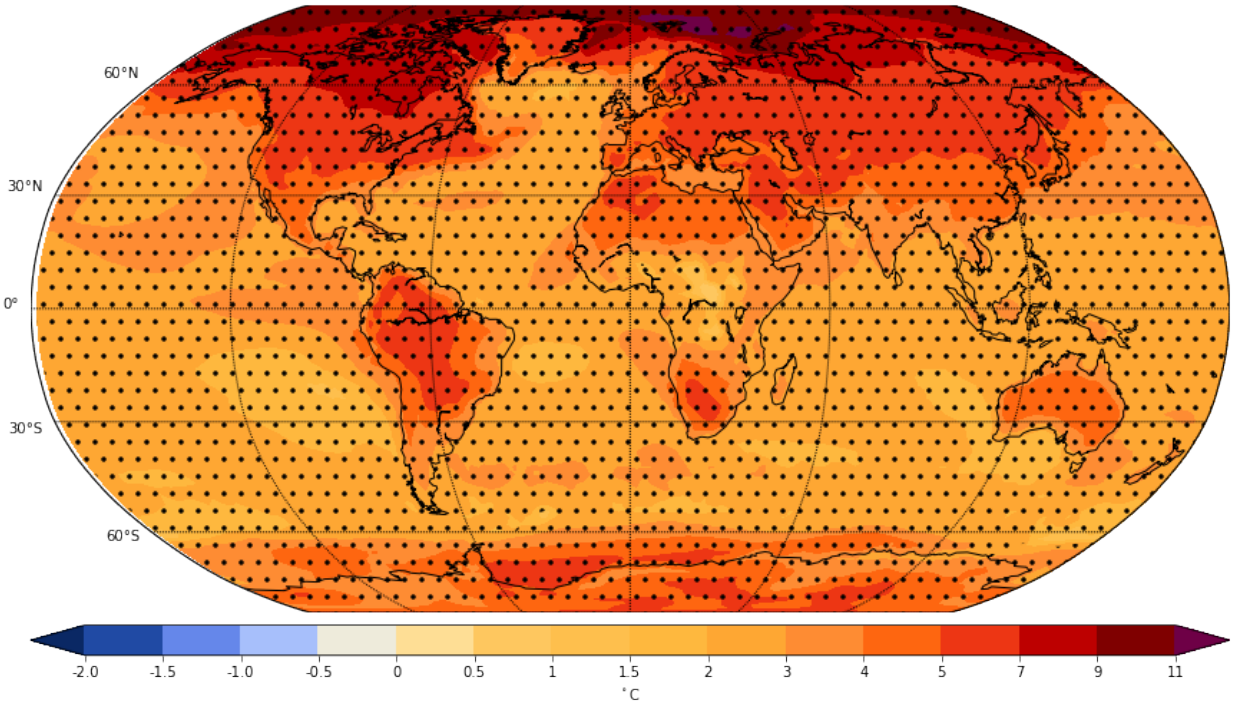

(b)

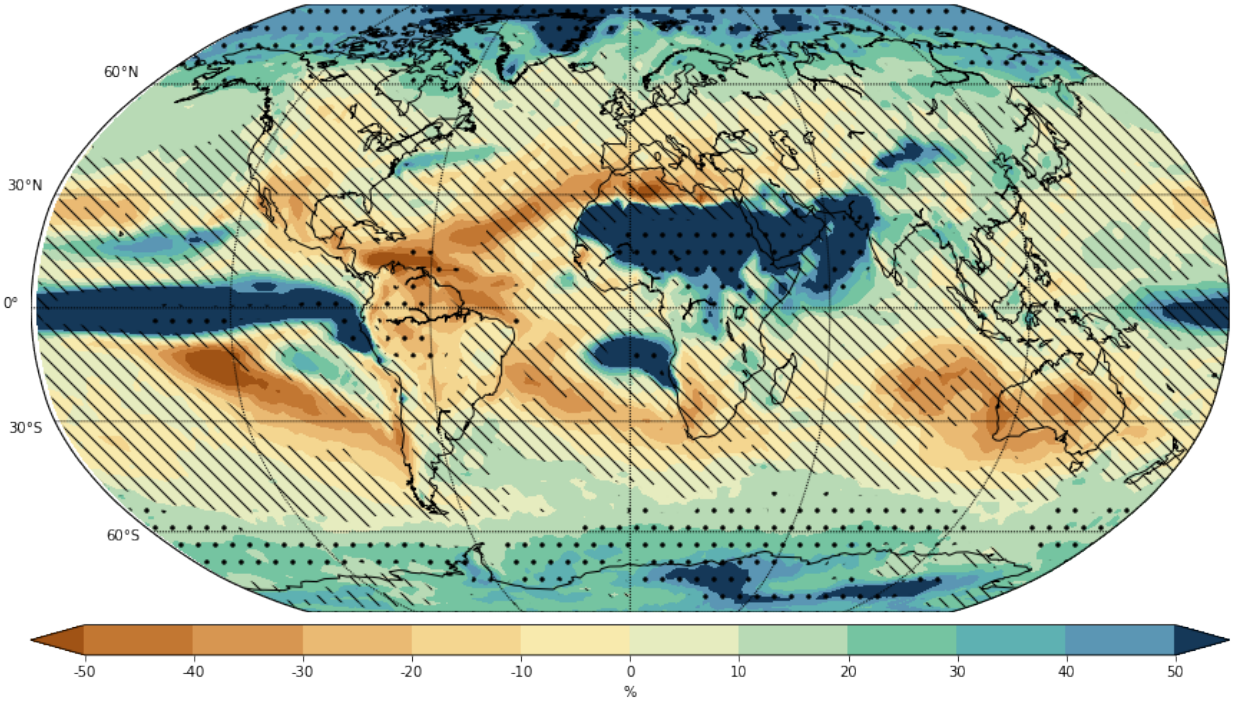

Fig. 10: (a) Annual mean 2 m temperature and (b) precipitation response according to the SSP585 scenario 2071-2100 compared to the historical period 1985-2014. Dotted (hatched) areas represent areas where simulated changes are larger than (smaller than) 2 standard deviations (1 standard deviation) of the internal variability based on yearly means of the 500-year control simulation.

4.2.2 Sea ice extent

Fig. 11 presents the simulated changes in sea-ice extent for Arctic (a, b) and Antarctic (c, d) during March and September according to piControl, historical and tier1 scenario experiments (i.e. ssp126, ssp245, ssp370 and ssp585). Aside from interannual fluctuations, overall behavior of all experiments is as expected; control experiments show insignificant negative trends with time, ranging from -0.0069 to -0.0027 Million km²/decade for Arctic and from -0.0044 to -0.0026 Million km²/decade for Antarctic during March and September, respectively. In comparison, historical and scenario experiments decline to various degrees over time in response to anthropogenic forcing. Here we present AWI-CM simulations for both Arctic and Antarctic regions for March and September over 250 years, from 1851 to 2100. These two months have been selected in order to cover the presumed maximum and minimum sea-ice extents for both hemispheres.

The strongest decline trend in sea-ice extent can be seen in the Arctic, during September (Fig. 11b). Based on all scenarios except for SSP126, there are at least periods of ice-free ocean in the Arctic starting from around 2050. In fact, SSP370 and SSP585 clearly suggest ice-free Arctic Septembers after this point. The observed September sea-ice extent according to AWI's Sea Ice Portal (Grosfeld et al., 2016) for 1979 to 2019 is shown (in purple) on top of AWI-CM outputs in

Fig. 11b, confirming that AWI-CM produces plausible average sea-ice extent which is in good agreement with the rate of Arctic sea-ice decline. According to the multi-model CMIP5 ensembles of September sea-ice extent, Arctic sea ice was melting even faster than predictions, even though observations remained within the first standard deviation of the models due to high internal variability of the participating models (Stroeve et al., 2015). In comparison, AWI-CM shows more adequate sensitivity to the forcings. Unlike multi-model CMIP5 ensembles, ice-free Septembers will be expected for not only ssp585 (corresponding to RCP 8.5 in CMIP5), but also for SSP245 (corresponding to RCP 4.5 in CMIP5) and SSP370 (new pathway). With additional observation years at hand, it is becoming more evident that the two sea-ice extent minima for years 2007 and 2012 are more likely to be assigned to natural variability than persistent trends.

Likewise, Arctic sea-ice extent during March has a continuously negative trend for historical and scenario experiments (Fig. 11a). This negative trend seems to be independent of the scenario until mid-21st century. However afterwards, sea-ice extent is stabilized at around 14 Million km² for SSP126 and SSP245. As detailed in Fig. 11a, scenarios incorporating higher radiative forcings (SSP370 and SSP585) predict accelerating decline of sea-ice extent. According to the high-end scenario of SSP585, by 2100, Arctic March sea-ice extent will decrease radically to half of its value at the beginning of the century.

IPCC AR5 (IPCC, 2014: Climate Change 2014: Synthesis Report p.48) reported low confidence in understanding the slight sea-ice extent increase in the Antarctic region, since the scientific reason behind it remained unexplained and CMIP5 models could not reconstruct such ascending behavior. According to IPCC AR5, it is suspected that this phenomenon is likely due to regional variability within the Antarctic (Stocker 2014, p.303). A study on individual CMIP5 models also suggested that although these models cannot replicate the observed Antarctic sea-ice extent trend, the observation still remains within the natural variability of better performing models (Turner et al., 2015). Bintanja (2013) showed that this sea-ice expansion could indeed be due to Antarctic sea ice shelf melting.

Consistent with CMIP5 models, AWI-CM predicts declining sea-ice extent for both September and March till the end of the century. Overall, interannual variability for Antarctic sea-ice extent is larger than Arctic, which confirms the findings of CMIP5 models by Turner et al. (2015). According to the current historical and scenario simulations, September Antarctic sea-ice extent will drop by about 2 Million km² from the end of historical experiment by about 2050. Afterwards, the SSP126 (i.e. the overshoot scenario) is the only one predicting a reverse trend for Antarctic sea ice toward expansion (Fig. 11d). Likewise, as illustrated in Fig 11c, March sea-ice extent in the Antarctic declines independent of the scenario until late 21st century. Only then, SSP245 and SSP126 suggest stabilization and a reverse trend respectively.

As discussed previously, the overall expansion of sea-ice extent, although of little statistical significance, has not been perfectly reproduced by models. Although simulations still remain within a reasonable range, the precise reasons for such difference is beyond the scope of this paper and remains unclear. AWI-CM Antarctic sea-ice extent also suggests a decline in response to anthropogenic forcing. Considering the relatively large natural variability of sea-ice extent in the Antarctic, further observations are needed in order to distinguish between natural variability

and a significant trend and obtain higher confidence in current predictions for Antarctic sea-ice extent.

Overall, AWI-CM-1-1-MR provides plausible sea-ice extent values for both Arctic and Antarctic. Except for internal variability, the piControl experiment remains constant in time as expected. The inter-ensemble variability for both historical and scenario (ssp370) experiments is small. This means that the results are robust against internal variability. The strong agreement with observations is another indicator of the model reliability and appropriate climate sensitivity with respect to sea-ice extent. The produced sea-ice extent reacts appropriately to different scenario experiments based on their associated radiative forcing. Generally, future sea-ice extent decline seems to be in line with the average of the CMIP5 models but even slightly stronger than predicted by them. IPCC AR5 reported September sea-ice extent reduction in 2081-2100 with respect to the average of the last 20 years of historical experiments (1986-2005) to be 43% for RCP2.6 and 94% for RCP8.5 (Stocker 2014, p. 92). Now, the September Arctic Sea-ice extent decline by the end of this century (2081-2100) with respect to the last 20 years of historical experiments (1995-2014) according to AWI-CM SSP126 and SSP585 are 64% and 99.99%. Both values are slightly larger than their respective percentiles in RCP2.6 and RCP8.5. These results imply higher confidence that the Arctic may become ice-free during September by the end of the 21st century.

(a)

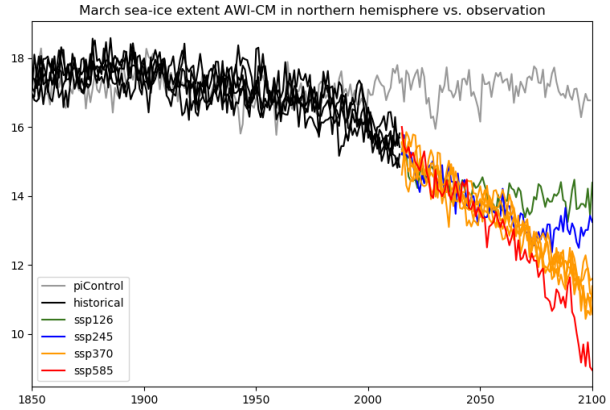

(b)

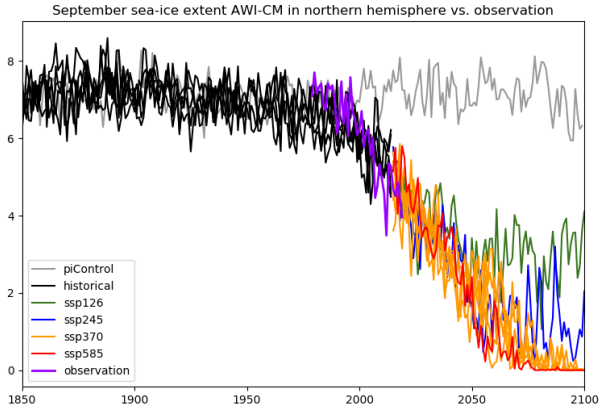

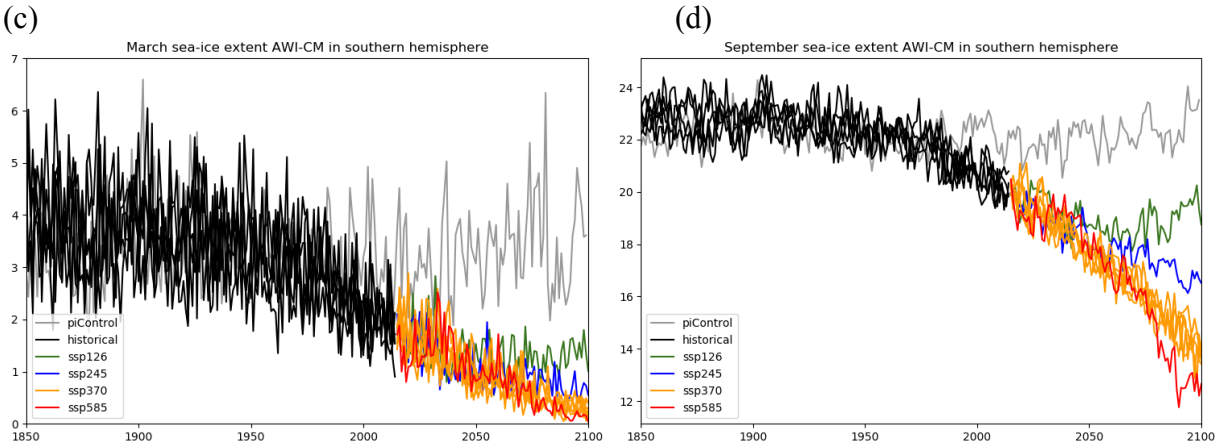

Fig. 11: (a) March and (b) September sea ice extent in the Arctic (Million km^2). (c) and (d) same as (a) and (b) but for the Antarctic region. For (b) the purple line indicates the observed sea ice extent from Meereisportal (Grosfeld et.al, 2016).

As the sea-ice extent, the decline of Arctic sea-ice thickness is also observed in the historical simulation during the freezing season (Fig. 12). Sea ice thickness in the Antarctic does not have such strong decline as that in the Arctic, but still shows slight decrease in recent decades. We compare the simulated ensemble mean thickness in the Arctic with recent satellite thickness data from CS2SMOS (Ricker et al., 2017), which is constructed by merging CryoSat-2 and SMOS thickness together using the optimal interpolation method. Sea ice thickness in the historical simulation falls well into the observed range from 2010 to 2013. Basin-scale observations for sea ice thickness in the Antarctic are rather limited. Evaluations against observations for Antarctic ice thickness are not possible at current stage.

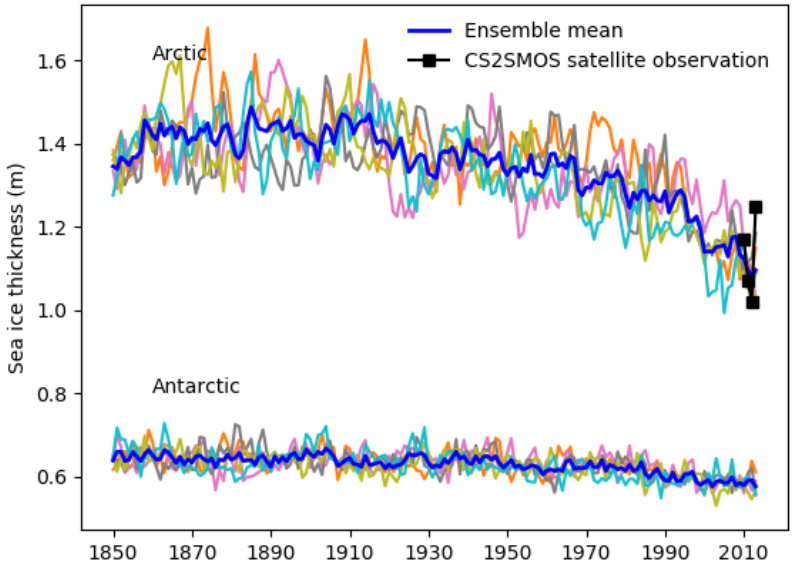

Fig. 12: Sea ice thickness in the historical simulation during the frozen season in the Arctic (December to March) and the Antarctic (May to September). The blue lines show the ensemble

mean of the 5 members indicated by different colors. CryoSat-2 and SMOS merged satellite thickness product CS2SMOS is shown by black squares.

4.3 Large scale circulation response

The mean sea level pressure (MSLP) response to increasing greenhouse gas concentrations (Fig. 13) is generally characterized by low anomalies over the polar regions and high anomalies in the southern mid-latitudes. Considering the geostrophic balance, this leads to an increase of the westerly flow in the northern and southern mid-latitudes mostly around 60° latitude. Over the Northern Hemisphere this increase is most pronounced in boreal autumn (SON) and winter (DJF). In the North Atlantic region the increase of the westerly flow is located further to the north compared to the CMIP5 ensemble mean as can be seen from Zappa and Shepherd (2017, their Fig. 1) while in the North Pacific region the location of the increase of the westerly flow is comparable. An intensified Aleutian low in boreal winter leads to a shift of the increased westerly flow over the North Pacific sector towards lower latitudes with a maximum around 45°N. Over the Southern Hemisphere the increased westerly flow is equally present in all seasons with a shift in the African sector towards lower latitudes in austral winter (JJA) and spring (SON).

For the 500 hPa geopotential height (z500), the general warming of the troposphere leads to increase everywhere (Fig. 14). However, there are regional differences in the magnitude of the increase. Over the Southern Hemisphere, z500 over Antarctica only increases by around 20 to 30 m but increases by more than 70 m over the mid-latitudes. The response pattern is similar to the MSLP response pattern. Also the shift of this pattern towards lower latitudes in austral winter and spring is present. Therefore, the response is barotropic. A barotropic response can also be seen over the North Pacific sector with the intensified Aleutian low both for z500 and for MSLP. However, over the Arctic the response is baroclinic with stronger z500 increases of more than 70 m in the high latitudes compared to the mid-latitudes along with the high-latitude MSLP decrease, at least in boreal winter and spring. This leads to a decrease in the intensity of the westerly flow when considering the geostrophic balance in the mid-troposphere while close to the surface the opposite is true. The reason for this is the pronounced Arctic Amplification leading to an increased thickness of the lower tropospheric layer. In the other seasons, z500 increases of more than 70 m are simulated both in the high and mid-latitudes.

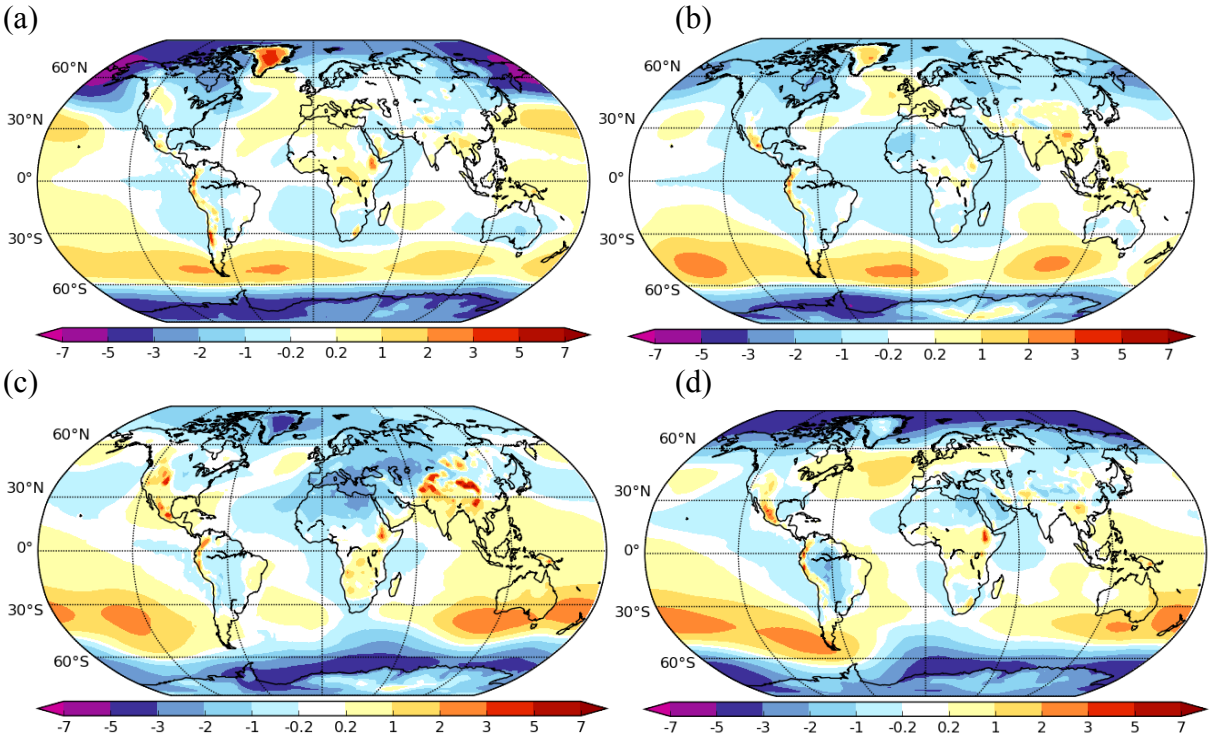

Fig. 13: Mean sea level pressure (MSLP) response SSP370 scenario ensemble mean over 5 realizations (2071-2100) compared to historical ensemble mean over 5 realizations (1985-2014). (a) DJF, (b) MAM, (c) JJA, (d) SON.

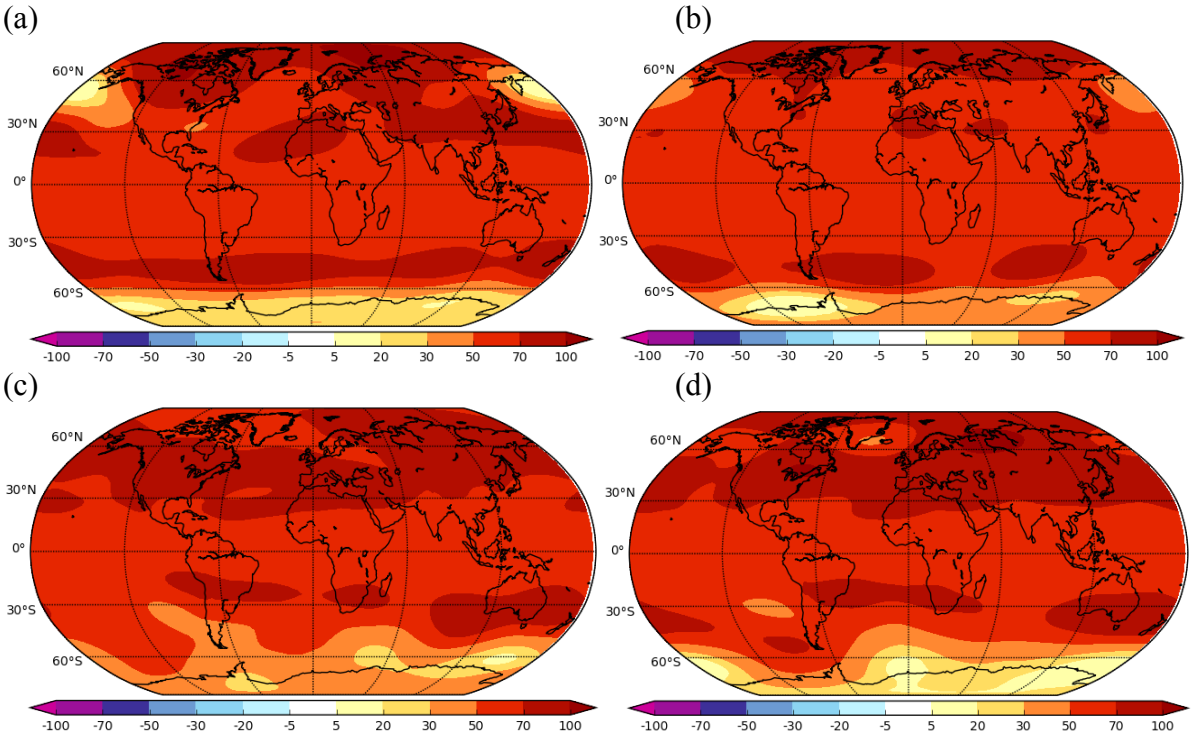

Fig. 14: 500 hPa geopotential height (z500) response SSP370 scenario ensemble mean over 5 realizations (2071-2100) compared to historical ensemble mean over 5 realizations (1985-2014). (a) DJF, (b) MAM, (c) JJA, (d) SON.

There is an ongoing discussion on how the waviness of the atmospheric flow will change in the future as a result of changes in the Arctic through Arctic Amplification and in the tropics through upper tropospheric warming. The contrasting effects have been termed a tug of war in the mid-latitudes which has led to various special issues in the literature, the most recent one: Nature Communications (2019). Will there be a more zonal flow with a decrease in the intensity of atmospheric waves implying less extreme warm and cold events or will the meridionality of the flow get stronger implying more extreme warm and cold events in the mid-latitudes? To answer this question from model simulations, various different objective indices have been defined. Cattiaux et al. (2016) defined the sinuosity index (SI) as the length of an isohypse of a specific value divided by the length of the 50°N latitude circle. If due to features such as cut-off lows there are separated isohypses of the specific value, the sum of the lengths of these isohypses is taken. The value of the isohypse is chosen as the area average of z500 over 30 to 70°N to accomodate for seasonal differences and climate change signals. If the SI equals to 1 the flow is zonal since the chosen isohypse is a straight line. The higher the SI, the stronger the meridional component of the atmospheric flow.

Fig. 15 shows the SIs computed for the piControl, historical, and scenario simulations. In all simulations, the waviness of the flow is more pronounced in winter and spring compared to summer and autumn. In addition, a pronounced interannual variability can be seen. With increasing greenhouse gas concentrations, there is a tendency towards a more zonal flow in boreal summer and autumn while in winter there is no robust change. This is consistent with the hypothesis of the tug-of-war: in boreal winter and spring the effect of Arctic Amplification can be seen in the zg500 response which is not the case for boreal summer and autumn. Therefore, in boreal summer and autumn the upper tropospheric warming in the tropics (not shown) leads to a more zonal flow while in boreal winter and spring there are compensating effects from Arctic Amplification and upper tropospheric tropical warming.

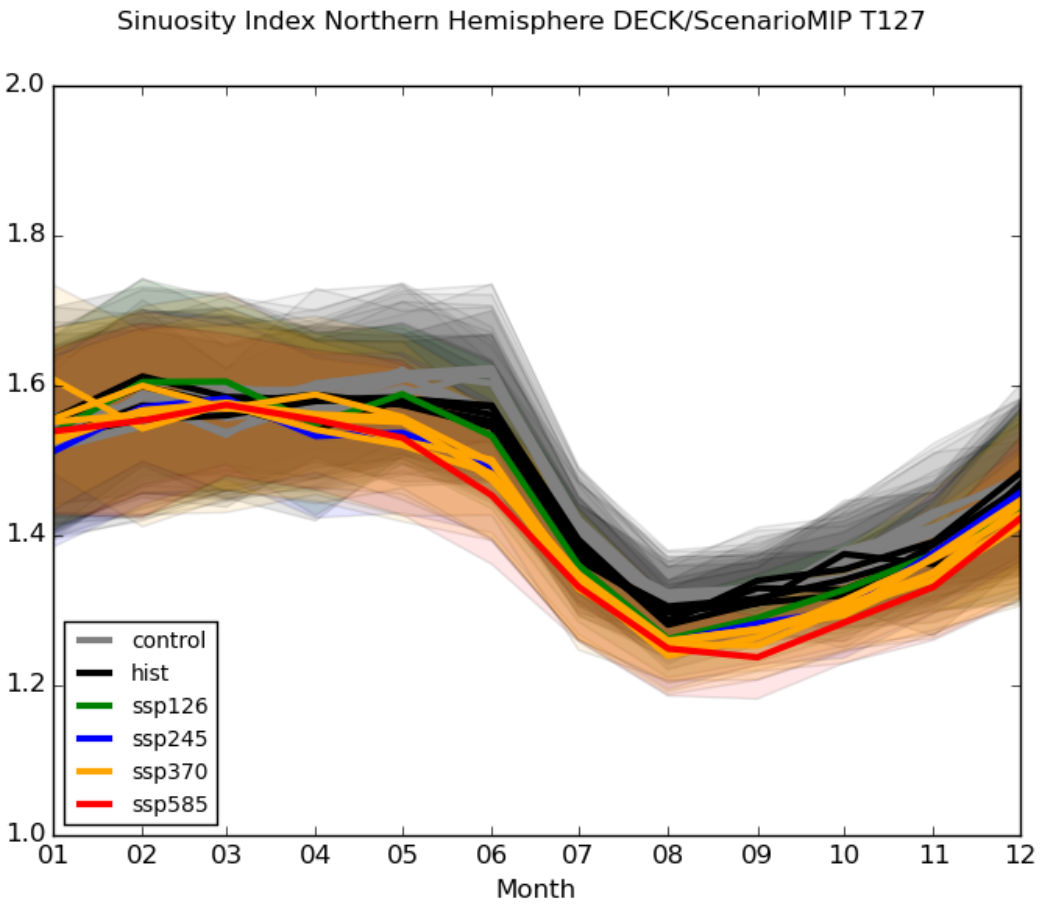

Fig. 15: Monthly sinuosity index in the Northern Hemisphere according to Cattiaux et al. (2016) from control, historical, and scenario simulations. Historical and scenario simulations are taken for the 30-year periods 1985-2014, and 2071-2100, respectively. From the control simulation all 30-year periods corresponding to the different ensemble members of historical and scenario simulations are considered resulting in multiple curves. The shaded areas represent the standard deviations of the 30 monthly sinuosity values for each simulation.

4.4 Ocean response

One important branch of the global ocean circulation is the Atlantic Meridional Overturning Circulation (AMOC). Transporting heat from the tropics to the northern North Atlantic, it has profound implications not only for the climate of north-western Europe but for the whole Northern Hemisphere and even leads to ocean heat transport from the South Atlantic to the tropics (Weijer et al., 2019). Figs. 16 and 17 show the maximum AMOC strength at 45°N for piControl, historical and scenario simulations as well as for piControl, 1pctCO2 and abrupt-4xCO2 simulations, respectively. In the case of a gradual increase of the greenhouse gas forcing (historical, scenario, and 1pctCO2 simulations), the AMOC strength at 45°N gradually decreases by around 25% until the end of the century with the high emission scenario SSP585 and by around 25% within 150 years in the case of the idealized 1pctCO2 simulation. In the case of the

low emission scenario SSP126, the AMOC strength at 45°N remains largely constant up to the end of the century. In the abrupt-4xCO2 simulation, the maximum AMOC strength decreases markedly by around 30% over the first 20 to 30 years. Over the remaining 120-130 years of the simulation, it slightly increases again by about 15% and thus reaches around 85% of the original strength.

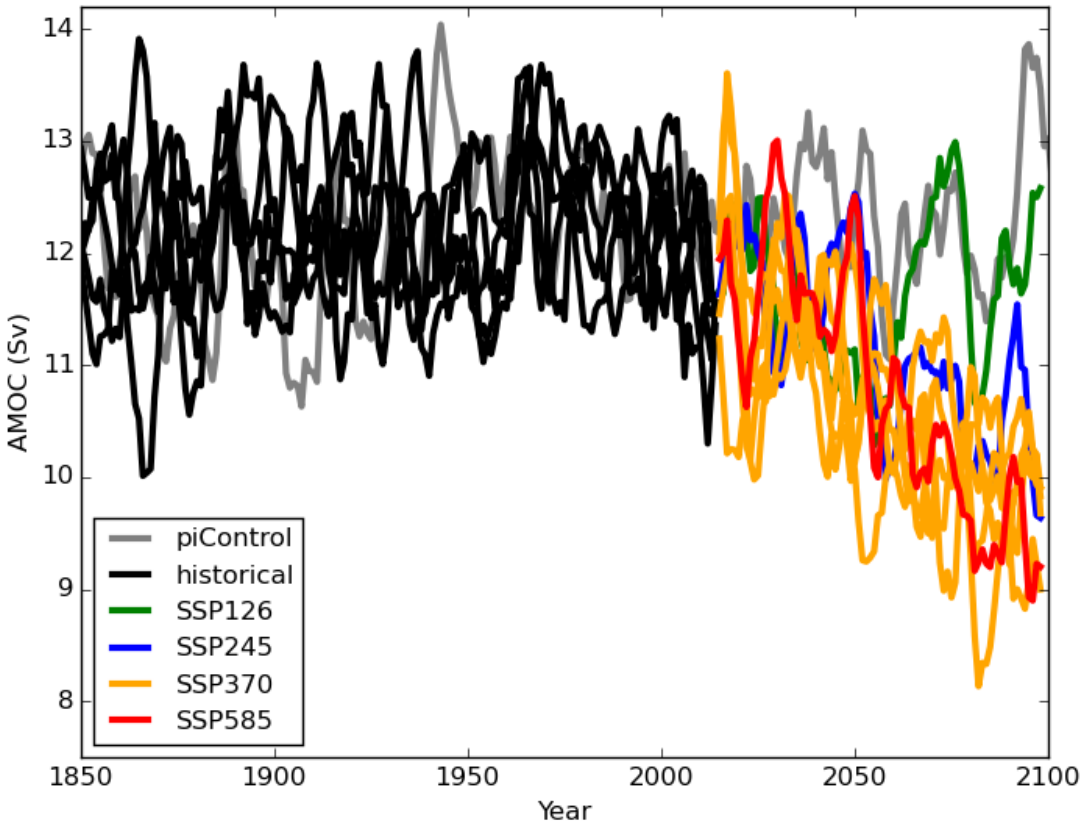

Fig. 16: 5-year running mean of maximum Atlantic Meridional Overturning Circulation (AMOC) (Sv) at 45°N for piControl, historical, and scenario simulations. For simplicity, the piControl simulation is only displayed corresponding to the 150-year branch-off point of the historical simulation ensemble member 1. Therefore, only one of the black lines from the historical simulations, namely historical simulation ensemble member 1, matches the piControl simulation AMOC in year 1850.

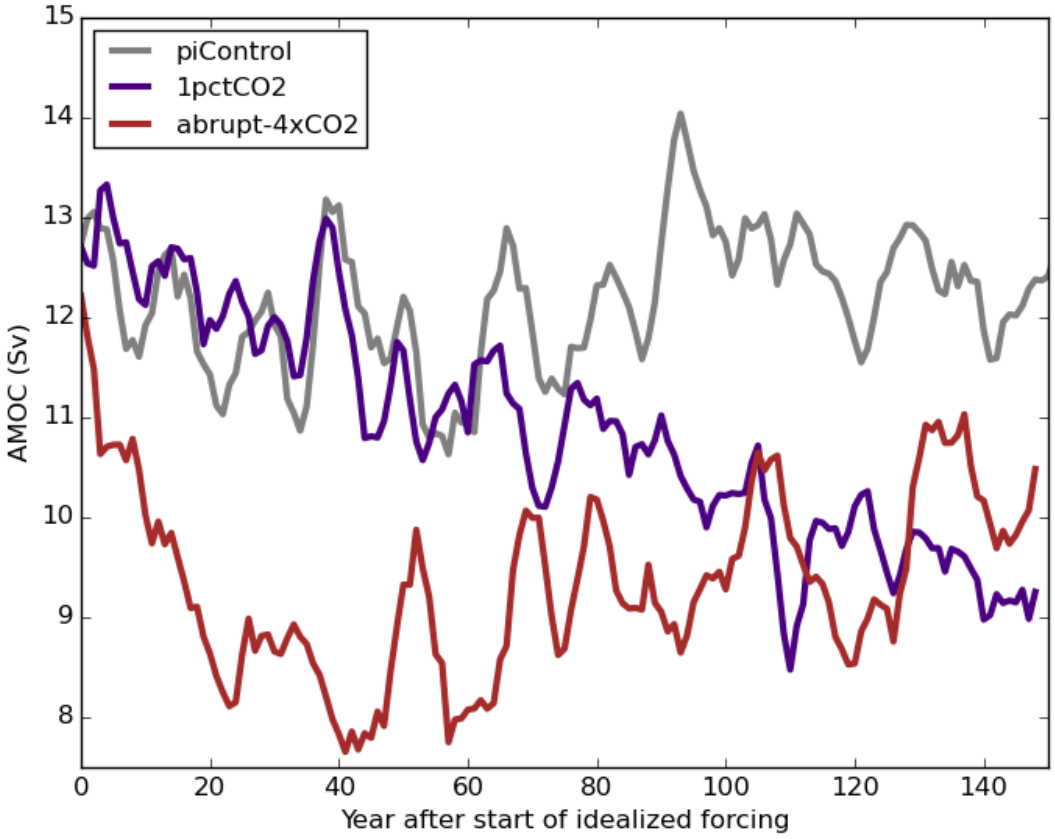

Fig. 17: 5-year running mean of maximum Atlantic Meridional Overturning Circulation (AMOC) at 45°N (Sv) for piControl and the idealized simulations 1pctCO2 and abrupt-4xCO2. Please note that the branch-off point for both idealized simulations is year 250 of piControl simulation. The year on the x-axis represents the year after this branch-off point and therefore the year after the start of the idealized forcing.

Table 4 shows the ocean volume transports through some key ocean straits averaged over the time period 1985-2014 in the historical runs and over the years 2071-2100 in the SPP370 runs. The values are the average over 5 ensemble members. The historical runs reasonably represent the volume transports through most of the ocean straits compared to the observational estimates. The volume transports through a few straits are underestimated, including the export transport from the Arctic Ocean to the North Atlantic measured at the David Strait, the Indonesian Throughflow, and the transport in the Mozambique Channel. The main reason for this is that the model resolution is not fine enough to resolve those narrow straits. In particular, the three main straits in the Canadian Arctic Archipelago (CAA) are only 10, 30 and 50 km wide at their narrowest locations, respectively, which cannot be well resolved with the mesh we used. Improved representation of the CAA straits, and thus of the ocean transport through the Davis Strait, is expected in our future coupled model configurations with higher ocean resolution, as indicated by high-resolution stand-alone simulations using FESOM (Wang et al., 2018; Wekerle et al., 2013).

The ocean volume transport shows a large response to the climate change SPP370 scenario at some ocean straits. The Florida Current decreases by about 15% at the end of the 21st century in the SPP370 scenario, which is consistent with the weakening trend of the AMOC described above. The ocean volume transport in the Indonesian Throughflow and the Mozambique Channel also decreases in the warming climate (by about 20%). This implies that the exchange between the Pacific, Indian and Atlantic Oceans will become weaker. The oceanic linkage between the North Atlantic and the Arctic Ocean, however, is strengthened significantly in the warming climate, as shown by the increase in the volume transport through the Barents Sea Opening (increase by about 40%). Together with the temperature increase in the Atlantic Water, this implies that oceanic heat supply from the North Atlantic to the Arctic Ocean will be increased in the future. As a consequence of ocean volume conservation, the excess ocean volume inflow through the Barents Sea Opening is balanced by an increased outflow through the Fram Strait.

In the warming climate the strength of the North Atlantic subpolar gyre (SPG) decreases, as shown by the increase in the sea surface height (SSH) in the SPG region (Fig. 18). The weakened SPG brings less Atlantic Water into the gyre circulation from the northeastern North Atlantic, which allows more Atlantic Water to continue to the north into the Nordic Seas. The enhanced northward flow is manifested by the increase in the SSH along the European coast. This can explain the stronger ocean volume transport through the Barents Sea Opening at the end of 21st century in the SPP370 scenario (Table 4).

Table 4: Ensemble mean of ocean volume transport (Sv) through different straits for the historical runs and spp370 runs. (Positive values mean north or eastward flows)

Straits	Historical run (1985-2014)	SSP370 (2071-2100)	Observations	References of observations
Fram Strait	-2.4	-3.1	-2.0 ± 2.7	Schauer et al. (2008)
Davis Strait	-0.6	-0.5	-1.6 ± 0.5	Curry et al. (2014)
Bering Strait	1.3	1.2	0.8 1	Roach et al. (1995) Woodgate (2008)
Barents Sea Opening	1.7	2.4	2	Smedsrud et al. (2010)

Drake Passage	169.2	170.1	136.7 ± 6.9 173.3 ± 10.7	Meredith et al. (2011) Donohue et al. (2016)
Mozambique Channel	-11.7	-9.4	-16.7 ± 8.9	Ridderinkhof et al. (2010)
Indonesian Throughflow	-12.4	-10.0	-15	Gordon et al. (2010)
Florida Bahamas Strait (28°N)	37.9	32.1	31.6	McDonagh et al. (2015)

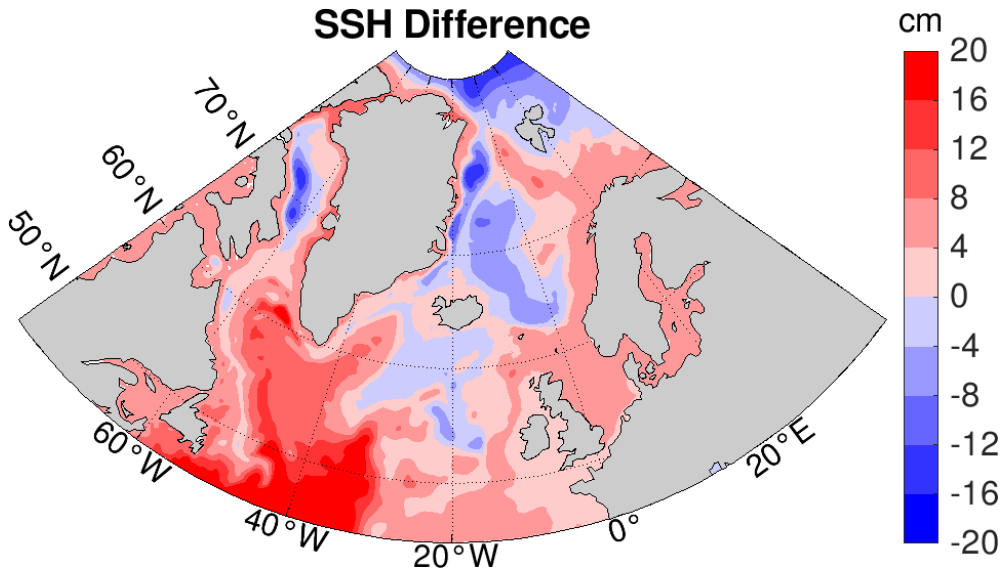

Fig 18: Difference of the sea surface height (SSH) between the mean over 2071-2100 (SPP370) and the mean over 1985-2014 (historical run) averaged over five ensemble members. Only the dynamical sea level part is considered in this plot, without the contributions from thermal expansion and water mass changes.

4.5 Changes in the energy budget

The global-mean net total TOA radiative imbalance remains, on decadal timescales, close to zero in the historical simulation until around 1970, after which it increases to ~0.7 W/m^2 around present-day (Fig. 19a, black solid curve), reflecting the uptake of heat by the climate system.

From there, the net total TOA radiative imbalance decreases gradually in the SSP126 scenario simulation, stabilizes at ~0.9 W/m^2 in the SSP245 scenario simulation, and continues to increase to up to 2.0 W/m^2 in the SSP370 and SSP585 scenario simulations toward the end of the 21st century (Fig. 19a, coloured solid curves). In contrast to the net total TOA radiation, its shortwave component exhibits a negative imbalance varying between 0.0 W/m^2 and -1.0 W/m^2 over the course of the historical simulation (Fig. 19a, black dashed curve), which implies an increased planetary albedo (Fig. 19b, black solid curve). The increased planetary albedo, particularly pronounced during the second half of the 20th century (+0.2%; the absolute simulated planetary albedo is ~28.9%), is not due to changes in surface albedo (Fig. 19b, black dashed curve), but is likely to the largest part due to anthropogenic aerosols that have compensated for a similarly strong positive longwave-radiative imbalance due to increased greenhouse-gas concentrations.

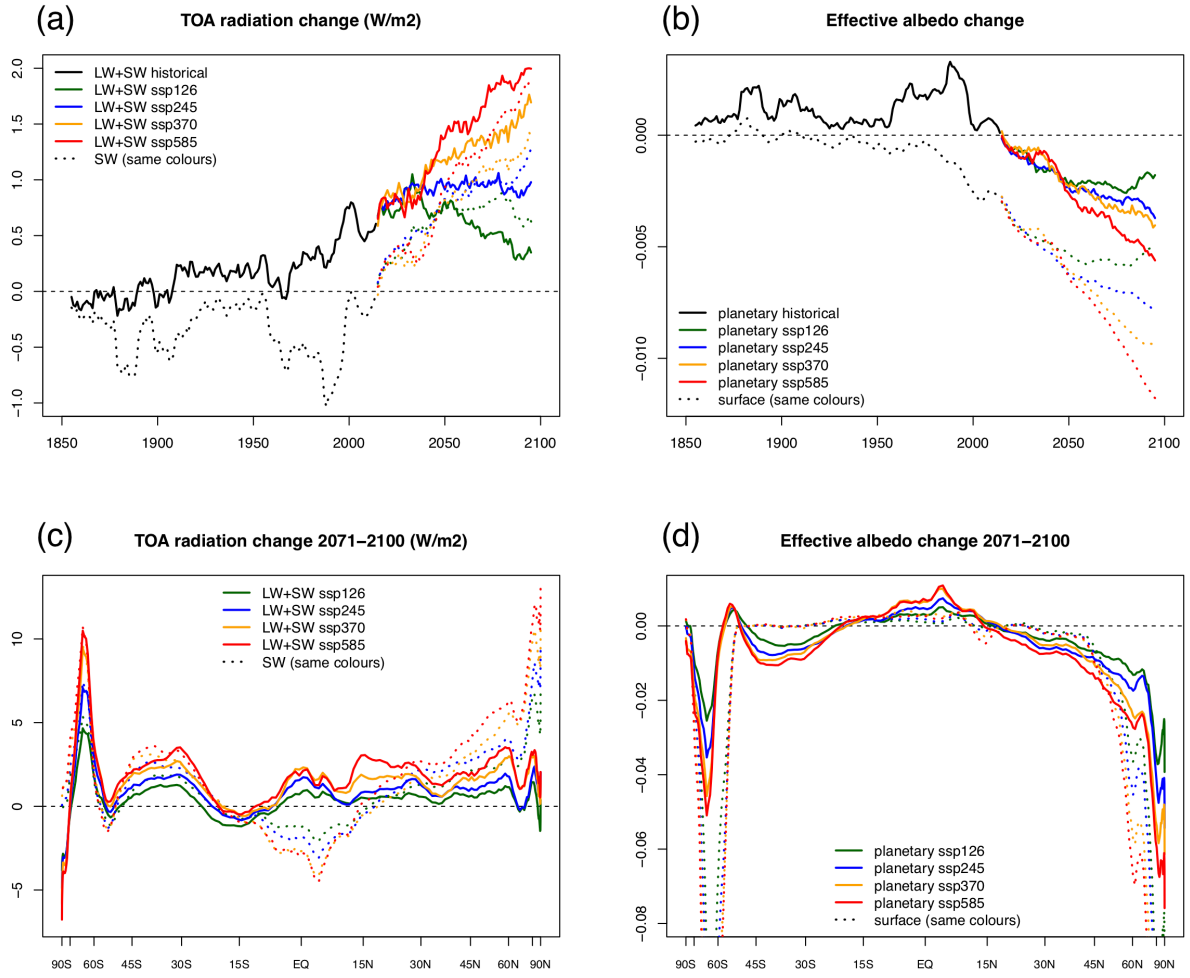

Fig. 19: Annual-mean changes in the energy budget, relative to piControl (delta approach). (a) Top of Atmosphere (TOA) net total (longwave (LW) + shortwave (SW); solid) and net shortwave (dashed) radiation time series after application of an 11-year running-mean, for the historical (black) and scenario (colours) simulations. Positive is downward. (b) Changes in the effective albedo diagnosed as upwelling divided by downwelling shortwave radiation at the TOA (planetary; solid) and at the surface (dashed). (c) and (d) same as (a) and (b) but as zonal means averaged over the period 2071-2100 (scenario simulations only), plotted against sin(latitude) to

reflect equal-area global contributions. Extreme negative values of effective surface albedo changes, reaching about -20% in both polar regions, are truncated in (d) to increase the visibility of changes in lower latitudes. Only the respective first ensemble member of the historical and SSP370 scenario simulations is shown.

While according to our simulations an increased planetary albedo has prevented a stronger warming of the climate system until present-day, the planetary albedo is projected to decrease and thus amplify the future warming in all scenarios (Fig. 19b, coloured solid curves and Fig. 19b, coloured dashed curves). The global-mean effective surface albedo, which seems to have played no major role until around 1980, is projected to decline by more than 1% (the absolute simulated effective surface albedo is ~13%) until the end of the century in the SSP585 scenario simulation and is thus a significant part of the projected positive shortwave feedback. Interestingly, the global-mean net shortwave radiation is projected to increase faster than the total radiation (Fig. 19a). This implies that, while reduced outgoing longwave radiation (OLR) has caused the warming until present-day, the OLR is projected to *increase* toward the end of the century: Due to the strong shortwave feedback, the positive influence of increasing temperatures on OLR is projected to outweigh the direct negative influence of increased greenhouse-gas concentrations on OLR. This behaviour has been found for most CMIP3 and CMIP5 models (Donohoe et al. 2014).

The surface albedo is decreasing particularly strongly in the regions with declining sea-ice extent, that is, the Southern Ocean (60S-70S) and the Arctic (north of 70N) (Fig. 19d, dashed curves). These changes are clearly reflected in the planetary albedo (Fig. 19d, solid curves), which however also reveals non-surface-related albedo changes in lower latitudes caused by cloud feedbacks. In particular, toward the end of the century the planetary albedo is projected to increase in the tropics between 15S and 15N (negative feedback) and to decrease in the subtropics (positive feedback) (Fig. 19d, solid curves).

While the surface-driven changes in the planetary albedo projected toward the end of the century are substantial in both polar regions, the positive net total TOA radiative imbalance is particularly pronounced over the Southern Ocean (Fig. 19c, solid curves). This is consistent with the relatively weak Antarctic and strong Arctic warming (Fig. 10a), leading to strongly enhanced upwelling longwave radiation in the Arctic but not in the Antarctic. This asymmetry in terms of polar amplification and TOA fluxes is consistent with the fact that the Southern Ocean temperature responds much more slowly to changes in atmospheric thermal forcing because of the spatial structure of the global Meridional Overturning Circulation (MOC), with circumpolar upwelling of unperturbed water masses in the south and downwelling in the north (Armour et al. 2016).

4.6 Changes in ENSO

Since ENSO is the largest signal of interannual variability on Earth and has many global impacts and teleconnections, an important question is whether the character of ENSO will differ under climate change. To assess this properly, we resort to the five SSP370 projections with AWI-CM

until the end of the 21st century. According to these simulations, when compared to the current probability distribution of Niño 3.4 SST anomalies (1985-2014), strong warm and cold SST anomalies become more likely under climate change by the end of this century (Fig. 20). Accordingly, neutral conditions or small SST anomalies are less frequent by 2071-2100. Interestingly, the seasonal cycle that has been subtracted to compute the SST anomalies within the Niño 3.4 box, consistently changes its shape under climate change in all ensemble members (Fig. 21): when subtracting the different annual means, a stronger positive (negative) peak in April/May (August-October) is evident, suggesting that seasonality within this region will likely increase until the end of the century. Concerning phase locking of SST anomalies to the seasonal cycle, their variability further increases throughout the whole year - particularly in July--October - and the previously clear phase locking relationship thus diminishes (Fig. 22). The result is a rather homogeneous distribution of monthly standard deviations by the end of the century: it lacks the U-shape that is hitherto present in observations for 1985-2014 (black points in Fig. 22) as well as in the full NOAA data dating back to 1870 (not shown).

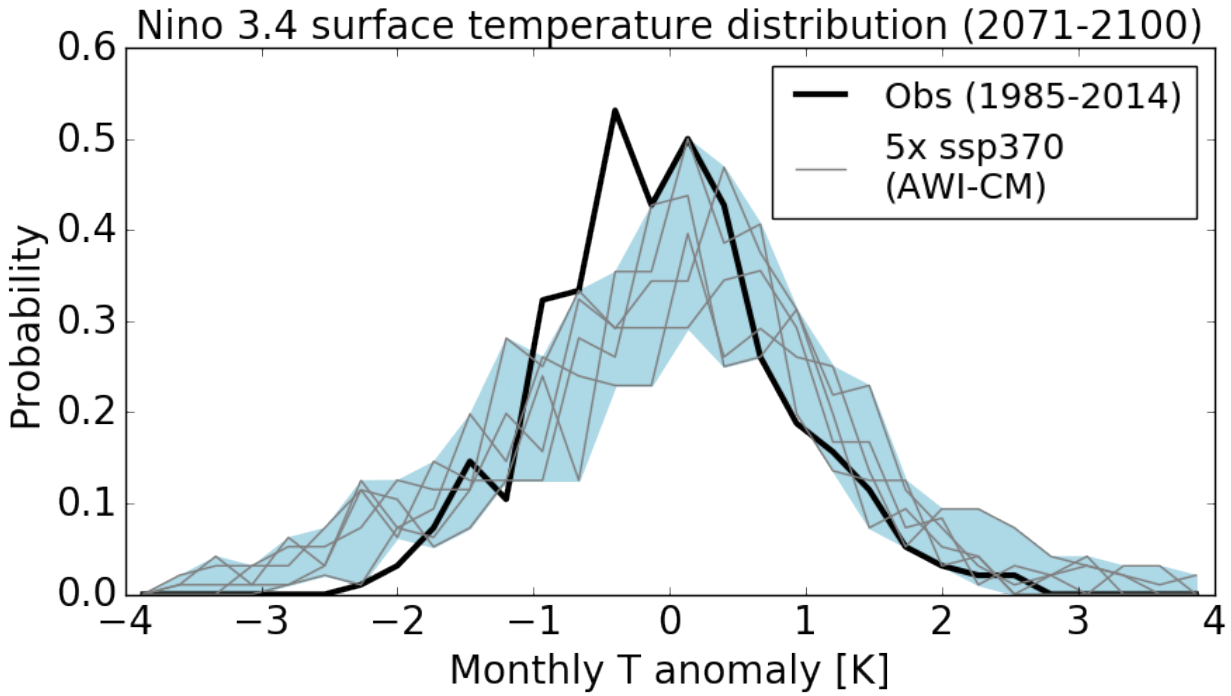

Fig. 20: Probability distribution function of sea surface temperature anomalies in the Niño 3.4 region for 2071-2100. Compared to 1985-2014, extreme anomalies become more likely while the probability of low to medium anomalies decreases. The range of the model results is shaded.

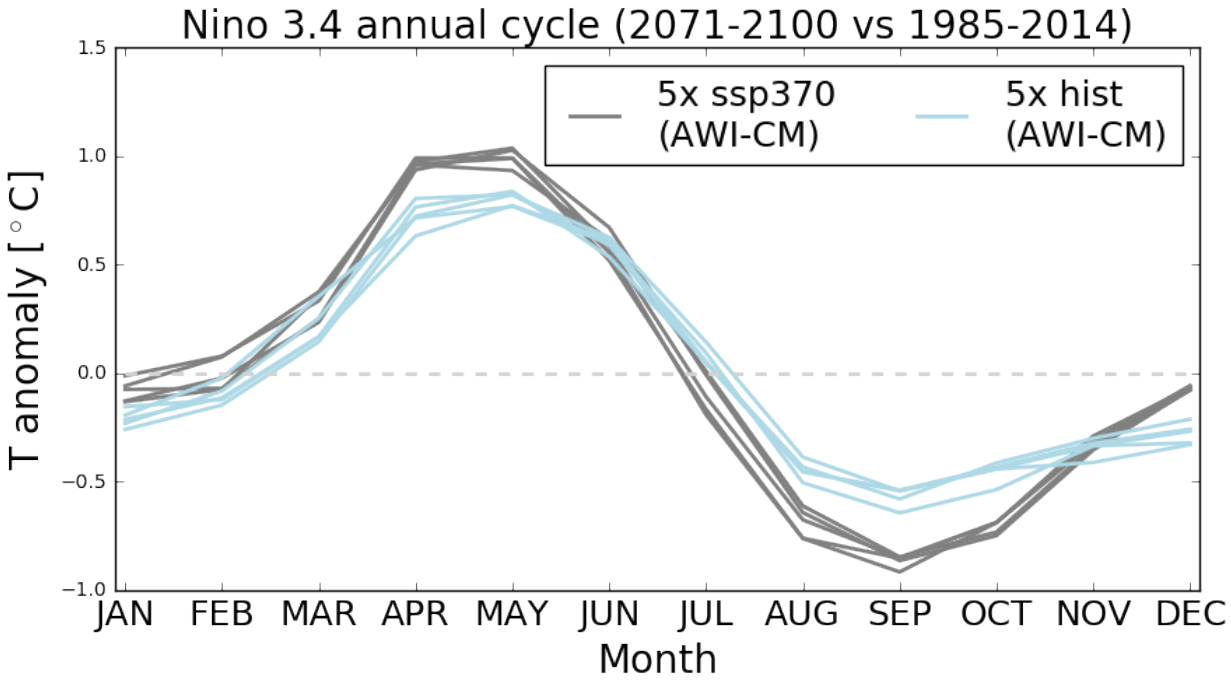

Fig. 21: The annual cycle within the Niño 3.4 box for recent (1985-2014) and future (2071-2100) conditions. 5 ensemble members each have been shown from the historical simulations (blue) and the ssp370 scenario (grey). The different annual means have been removed to highlight the consistently different shape of the annual cycles.

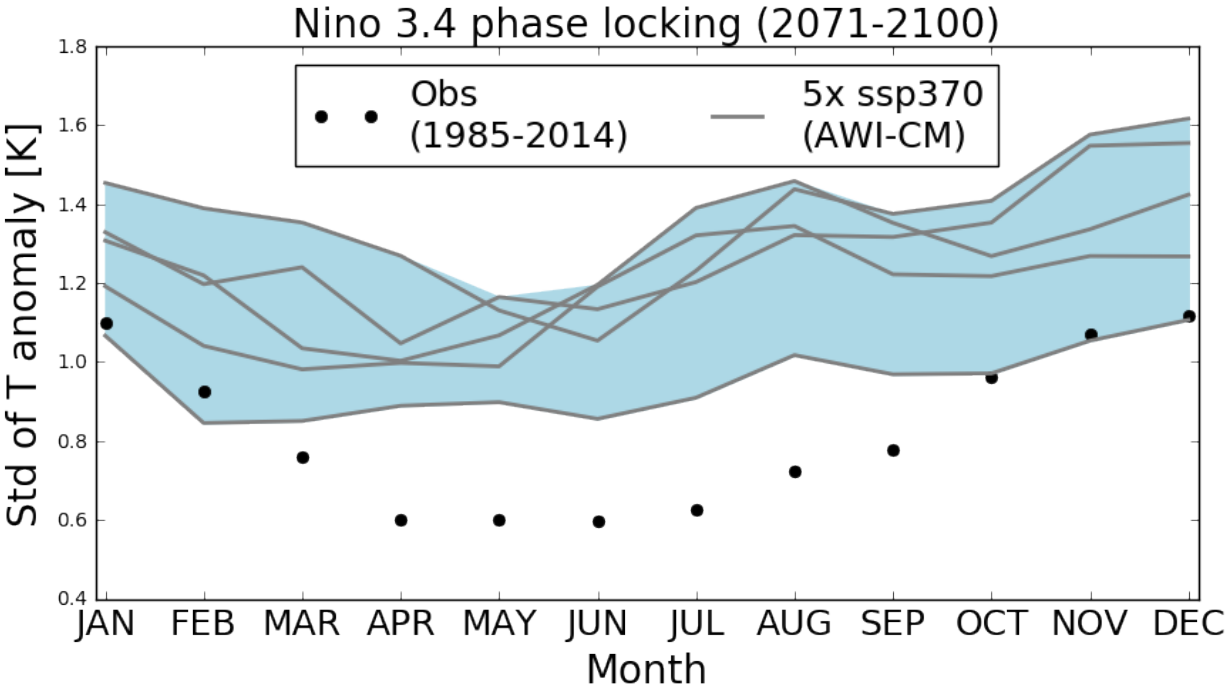

Fig. 22: Seasonal phase locking of temperature anomalies in the Niño3.4 region for 2071-2100. Black dots give the monthly standard deviation of the observed Niño3.4 index (1985-2014) by

NOAA; grey lines give the standard deviations of the simulated Niño3.4 indices for the five ssp370 ensemble members. The range of the model results is shaded in light blue.

5 Discussion and conclusions

AWI-CM, described in this study, contributes to the diversity of climate models since it uses an unstructured mesh approach for the sea ice-ocean component. It is promising that biases in our model tend to be less pronounced than in models used for the previous Climate Model Intercomparison Project 5 as shown by objective performance indices. It is found that our model shows very similar response features compared to the multi-model ensemble of CMIP5 simulations, both in patterns and in magnitude. Features such as a strong Arctic Amplification along with a weak Antarctic Amplification, Arctic wetting (Bintanja and Selten, 2014), subtropical drying, increased frequency of extreme La Niña & El Niño events (Cai et al., 2015), and weakening Atlantic Meridional Overturning Circulation are very similar to the previous simulations. Therefore, the statement that some of the climate change features are generally robust against the model formulation and that the commonly used delta approach to deduce the climate change signal from the difference between historical / scenario simulations on the one hand and the control simulation on the other hand can be strengthened.

Compared to the multi-model mean over CMIP5 simulations, the equilibrium climate sensitivity is very similar in our model (3.2°C). The transient climate response is 10-15% higher in our model (2.1°C compared to 1.8°C in the multi-model mean over CMIP5 simulations). CMIP6 simulations tend to show a higher climate sensitivity compared to CMIP5 simulations (Hausfather, 2019), although not all planned simulations from all models are available at the time of writing. A quarter of the available CMIP6 simulations have a higher sensitivity than any of the models featured in CMIP5. Arctic sea ice extent decline by the end of the 21st century is stronger than the multi-model mean over CMIP5 simulations, suggesting a higher likelihood of an ice-free Arctic by 2050. Surface albedo changes, in particular in both polar regions where sea ice declines, are projected to contribute substantially to a strong positive shortwave feedback. It is thus surprising that a recent geoengineering study based on AWI-CM has revealed a very small impact of an intervention in the Arctic ice-albedo feedback on temperatures outside the Arctic (Zampieri and Goessling 2019).

While the Arctic sea ice extent trend is still slightly smaller in our model simulation compared to observations over the last few decades, the global mean temperature increase is slightly larger compared to observations both over the last 30 and over the last 150 years. This may hint at an underestimation of Arctic Amplification in our simulations or that multi-decadal internal variability is superimposed on the observed Arctic climate change. The latter hypothesis is supported by Kay et al. (2011) stating that half of the strong negative Arctic sea ice trend from 1979 to 2005 is explained by internal variability and the other half by the climate change signal.

The AMOC decreases by around 25% until the end of the century according to the AWI-CM SSP585 scenario simulation, which is less than the multi-model average value of 40% calculated from CMIP5 models and Earth System Models of Intermediate Complexity (EMICs, Weaver et al., 2012). A more realistic representation of western boundary currents and the Agulhas leakage in higher-resolution ocean models has been found to stabilize the AMOC (e.g. Biastoch et al.,

2018, Sein et al., 2018, Weijer et al., 2019). Considering that AWI's CMIP6 configuration features one of the highest spatial ocean resolutions among the CMIP6 models (see http://rawgit.com/WCRP-_CMIP/CMIP6_CVs/master/src/CMIP6_source_id.html), this effect may explain the stronger AMOC stability in our simulations compared to the ensemble discussed by Weaver et al. (2012).

The AWI-CM model data is freely available through the Earth System Grid Federation (ESGF) and includes not only the here described DECK and ScenarioMIP experiments (Semmler et al., 2018). At the time of writing, AWI-CM results from the Polar Amplification Model Intercomparison Project (PAMIP, Smith et al., 2019) and results with AWI-CM-1-1-HR from the High Resolution Model Intercomparison Project (HighResMIP, Haarsma et al., 2016) are available as well (Semmler et al., 2017; Semmler et al., 2019). Furthermore, data publications of AWI-CM simulations are planned for OMIP (Griffies et al., 2016) and PMIP (Kageyama et al., 2018).

Appendix

A1 Postprocessing software for cmorization and easy use of unstructured mesh data for analysis

For the ocean cmorization, the user is being guided to easily notice any incompatibilities between the actual available output and the designated data request tables. In this conversion process, the most time consuming step would be any changes to the bulk variable data itself, as metadata can generally be applied quickly and independent of the data amount in one file. The time/resources required for changes in the variable data on the other hand will theoretically increase linearly with the size of the mesh and the frequency of the data. Therefore we had to avoid all steps and utilities which cannot alter data in-place, e.g. where no auxiliary file or memory allocation is required.

The overall requirements for a complete CMIP6 formatted file set can be somewhat intriguing due to its complexity (data request (DR), naming conventions, controlled vocabularies, Earth System Grid Federation (ESGF) requirements, model details). Therefore our CMIP6 CMOR setup has been realized via a compact and human-readable setup domain-specific language (DSL). This setup can be executed shared-memory-parallel per conversion task on a HPC system right where the data is stored.

The following steps are necessary where the duration scales with the grid size and is limited by the I/O speed of the filesystem (i.e. changes of the bulk data):

- frequency change (e.g. due to requirements in the DR)
- unit change (e.g. from DR 1.0.3 to DR 1.0.27 some temperature variables changed the unit from deg C to K). Technically not a problem, but requires to I/O all affected data.
- data concatenation (merge)
- compression (e.g. different as the ESGF)
- file format change (e.g. as required by ESGF)

A necessary requirement for using the model data for scientific research is the availability of tools that are able to perform basic pre- and post-processing operations on model output. For ocean models on structured grids, a wide selection of tools is available; for the new generation of global ocean models formulated in unstructured meshes, however, no existing off-the-shelf packages exist. Therefore, we have created a set of python-based analysis and visualization tools for FESOM - pyfesom (https://github.com/FESOM/pyfesom). The pyfesom repository contains python library and command line tools that allow to perform basic data analysis and visualisation of FESOM data, and provide ways to interpolate FESOM data to regular grid. There is also a documentation with description of command line tools and set of Jupyter Notebooks with examples of library usage. Moreover, we have developed the R package spheRlab (https://github.com/FESOM/spheRlab) which facilitates the analysis and visualization of unstructured-mesh data, including functions for the generation of grid description files that enable full compatibility of FESOM data with the more widely used Climate Data Operators (CDO; https://code.mpimet.mpg.de/projects/cdo).

Atmospheric data has been cmorized with an approach developed by the German Climate Computing Centre (DKRZ). All the FESOM ocean data has also been cmorized in a CDO-compatible manner. To give an example, a typical file is the unstructured potential ocean temperature in *thetao_Omon_AWI-CM-1-1-MR_historical_r1i1p1f1_gn_185001-185012.nc*. A horizontal conservative remapping of this file to a 1°x1° regular grid ("r360x180") from the command line is a one-liner and as simple as

cdo remapycon,r360x180 thetao_Omon_input.nc thetao_Omon_remapped2D.n

where we shortened the input file name to *thetao_Omon_input.nc* for brevity. An analogous command results in a bilinear interpolation by replacing "remapycon" with "remapbil". If many years need to be remapped, it is advisable to generate the interpolation weights only once *(cdo genycon,r360x180 thetao_Omon_input.nc weights_unstr_2_r360x180.nc*) and to re-use them for all subsequent remapping commands:

cdo remap,r360x180,weights_unstr_2_r360x180.nc thetao_Omon_input.nc thetao_Omon_remapped2D.nc

Furthermore, additional vertical interpolation to a set of different depth levels can be achieved via, e.g.,

cdo intlevel,10,20,30,50,75,100,125,150,200,250,300,400,500,600,700,800,900,1000,1100,1200,1300,1400,1500, 1750,2000,2500,3000,3500,4000,4500,5000,5500 thetao_Omon_remapped2D.nc thetao_Omon_remapped3D.nc

A2 Imbalances and remaining drift at the end of the pre-industrial control simulation

In the last 100 years of the 500 year piControl simulation, which followed the 500 year spinup simulation, there are still imbalances in the top-of-atmosphere (TOA) and net surface radiation. Averaged over these 100 years the TOA radiation imbalance amounts to 0.34 W/m^2 whereas the net surface energy flux consisting of radiation and turbulent heat fluxes amounts to 0.84 W/m^2.

Given that changes in the atmospheric energy content on this time scale are much smaller, the discrepancy implies an unphysical atmospheric energy non-conservation of about 0.5 W/m^2.

The gradual energy loss of the ocean over the same time period, diagnosed from changes in the 3D ocean temperature (and sea-ice mass changes), corresponds to a global surface energy flux of -0.01 W/m^2. The deviation from the atmospheric surface flux imbalance by 0.85 W/m^2 cannot be explained by changes in the continental heat content, but points to further deviations from energy conservation that can be related to mismatching grids and coastlines between the model components, inconsistent treatment of temperature, precipitation and runoff (Mauritsen et al. 2012), or other inconsistencies. The atmosphere-related and the surface-related non-conserving energy terms partly compensate each other, resulting in an overall unphysical energy sink of -0.35 W/m^2, and both of them are relatively constant over all simulations (when averaged over decades and longer; not shown).

To diagnose the ocean drift further, Fig. A1 shows the Hovmöller diagrams for the global profiles of oceanic potential temperature and salinity for the last 400 years of the control simulation. The amplitude of the drift hardly reaches 0.15 °C for temperature and 0.05 psu for salinity, respectively, indicating that the system is close to its quasi equilibrium state. The drift in temperature is characterized by four main zones localized at depths of 500, 1,500, 3,000 and 4,500 m. The drift in salinity is characterized by two main zones at depths of 500 and 2,000 m. From inspecting the spatial distribution of the drift (not shown) we conclude that the upper zone at 500 m stems primarily from the overall cooling and freshening of the ocean. The anomalous zone between 1,500 m and 2,000 m comes from the Mediterranean outflow which spreads into the southern North Atlantic being too warm and salty. At 3,000 m we observe that the Atlantic and Pacific Oceans become cooler while Indian and Southern Oceans show positive trends in temperature. Simultaneously, salinity in the North Atlantic shows a negative trend at this depth, in terms of density partly compensating the warming signal there. Everywhere else at this depth there is a positive drift in salinity, most pronounced in the Indian Ocean. Finally, the deepest zone of temperature increase at ~4,500 m stems from a warming trend in the Southern Ocean. Although the spatial pattern of non-zero temperature changes implies a weak redistribution of heat and salinity remaining, we overall conclude that the system is close to a quasi equilibrium state.

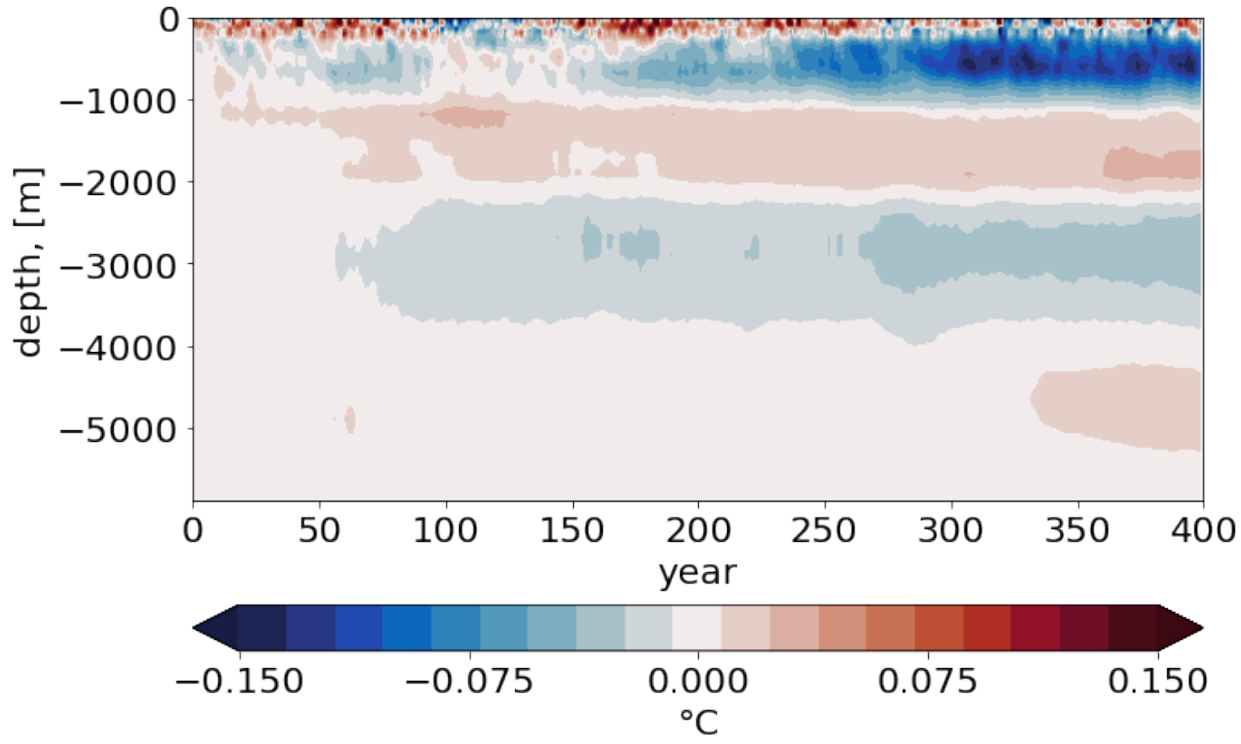

(b)

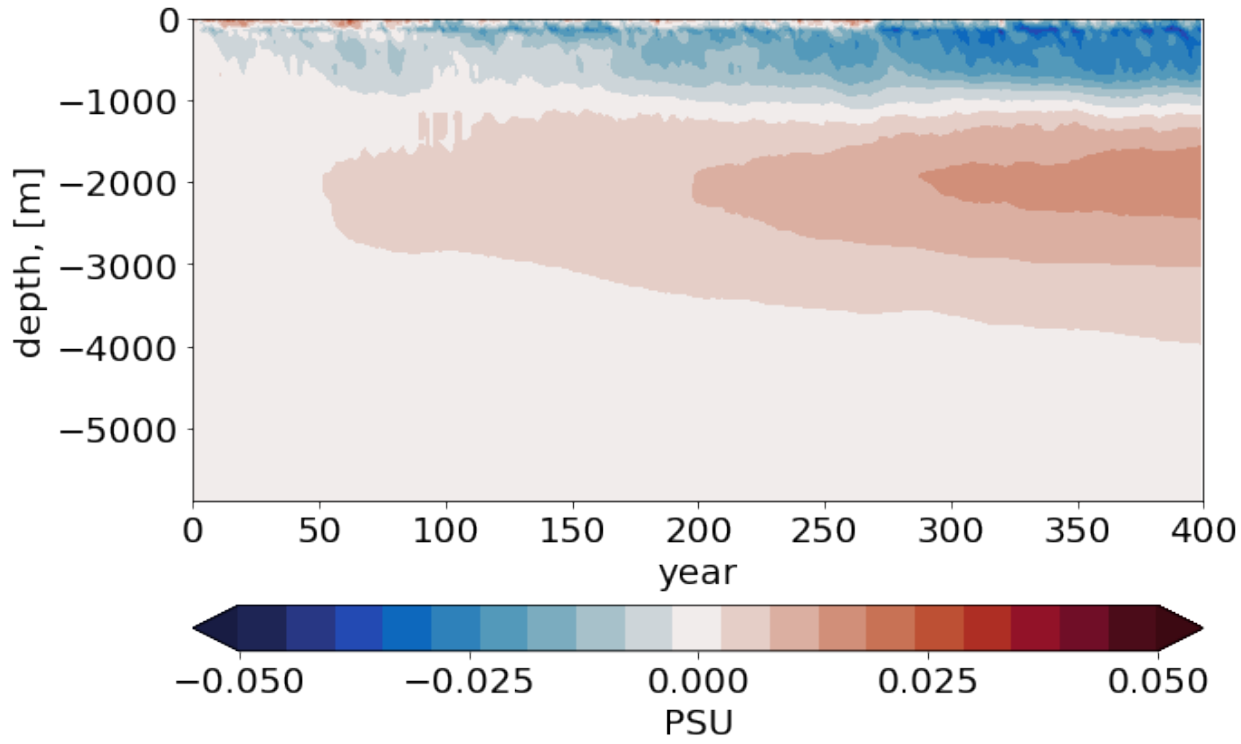

Fig. A1: Vertical profiles of ocean temperature and salinity in the last 400 years of the 500 years of piControl simulation (relative to the beginning of this 400 year time period). The last 400 years cover all simulations branched off since the first branch-off point is in year 150 of the piControl simulation, i.e. 350 years before the end of the piControl simulation (see Table 1). The

drift during the years to be compared between idealized, historical, and scenario simulations on one hand and control simulation on the other hand is clearly smaller than the climate change signal described in section 4.4.

Acknowledgments and Data Availability Statement

We used the Niño3.4 index as provided by NOAA on their website at https://www.esrl.noaa.gov/psd/gcos_wgsp/Timeseries/Nino34/. H. F. Goessling and L. Mu acknowledge the financial support of the Federal Ministry of Education and Research of Germany in the framework of the research group Seamless Sea Ice Prediction (SSIP; Grant 01LN1701A). N. Khosravi and C. Hinrichs have received funding from the European Union's Horizon 2020 Research and Innovation programme through grant agreement No. 727862 APPLICATE. This paper is a contribution to the projects S1 (Diagnosis and Metrics in Climate Models) and S2 (Improved parameterizations and numerics in climate models) of the Collaborative Research Centre TRR 181 "Energy Transfer in Atmosphere and Ocean" funded by the Deutsche Forschungsgemeinschaft (DFG, German Research Foundation) – project no. 274762653. D. Sein was supported by EC Horizon 2020 project PRIMAVERA under the grant agreement no. 641727, the state assignment of FASO Russia theme No. 0149-2019-0015. Q. Wang and D. Sidorenko were supported by the Helmholtz Climate Initiative REKLIM (Regional Climate Change). The simulations were performed at the German Climate Computing Center (DKRZ). We thank the Max-Planck-Institute for Meteorology in Hamburg (MPI) for providing us with the model code and for the fruitful discussions with various colleagues from this institute. All data are available on the Earth System Grid Federation (ESGF) (Semmler et al., 2018).

References

Armour, K., Marshall, J., Scott, J. et al. (2016) Southern Ocean warming delayed by circumpolar upwelling and equatorward transport. Nature Geosci, 9, 549–554. doi:10.1038/ngeo2731

Biastoch, A., Sein, D. V., Durgadoo, J. V., Wang, Q. and Danilov, S. (2018). Simulating the Agulhas system in global ocean models – nesting vs. multi-resolution unstructured meshes. Ocean Modelling, 121, pp. 117-131. doi:10.1016/j.ocemod.2017.12.002

Bintanja, R., et al. "Important role for ocean warming and increased ice-shelf melt in Antarctic sea-ice expansion." Nature Geoscience 6.5 (2013): 376.

Bintanja, R., Selten, F. Future increases in Arctic precipitation linked to local evaporation and sea-ice retreat. *Nature* **509,** 479–482 (2014) doi:10.1038/nature13259.

Cai, W., Santoso, A., Wang, G. *et al.* (2015) ENSO and greenhouse warming. *Nature Clim Change* 5, 849–859, doi:10.1038/nclimate2743

Cattiaux, J., Peings, Y., Saint-Martin, D., Trou-Kechout, N., and Vavrus, S. J. (2016) Sinuosity of midlatitude atmospheric flow in a warming world. Geophysical Research Letters, https://doi.org/10.1002/2016GL070309.

cmip6-cmor-tables https://github.com/PCMDI/cmip6-cmor-tables access date 2019/12/19

Curry, B., Lee, C. M., Petrie, B., Moritz, R. E., and Kwok, R. (2014) Multiyear Volume, Liquid Freshwater, and Sea Ice Transports through Davis Strait, 2004–10, J. Phys. Oceanogr., 44, 1244-1266.

Danilov S, Kivman G, Schröter J (2004) A finite-element ocean model: principles and evaluation. Ocean Model 6(2):125–150.

Donohoe, A., Armour, K.C., Pendergrass, A.G. and Battisti, D.S., 2014. Shortwave and longwave radiative contributions to global warming under increasing CO2. Proceedings of the National Academy of Sciences, 111(47), pp.16700-16705.

Donohue, K.A., Tracey, K.L., Watts, D.R., Chidichimo, M.P., Chereskin, T.K., 2016. Mean Antarctic circumpolar current transport measured in drake passage. Geophys. Res. Lett. 43, 11760-11767.

Eyring, V., Bony, S., Meehl, G. A., Senior, C. A., Stevens, B., Stouffer, R., J., Taylor, K. E., 2016: Overview of the Coupled Model Intercomparison Project Phase 6 (CMIP6) experimental design and organization, Geosci. Model Dev., 9, 1937–1958, https://doi.org/10.5194/gmd-9-1937-2016.

Gent, P. R. and McWilliams, J. C.: Isopycnal mixing in ocean circulation models, J. Phys. Oceanogr., 20, 150–155, 1990.

GISS, 2019: GISS surface temperature analysis GISTEMP v4. Available online at https://data.giss.nasa.gov/gistemp/.

Good, S. A., M. J. Martin and N. A. Rayner, 2013. EN4: quality controlled ocean temperature and salinity profiles and monthly objective analyses with uncertainty estimates, Journal of Geophysical Research: Oceans, 118, 6704-6716, doi:10.1002/2013JC009067.

Gordon, A., Sprintall, J., Van Aken, H., Susanto, D., Wijffels, S., Molcard, R., Ffield, A., Pranowo, W., and Wirasantosa, S. (2010) The Indonesian throughflow during 2004–2006 as observed by the INSTANT program, Dynam. Atmos. Oceans, 50, 115-128.

Gregory, J. M., Ingram, W. J., Palmer, M. A., Jones, G. S., Stott, P. A., Thorpe, R. B., Lowe, J. A., Johns, T. C., Williams, K. D. (2004) A new method for diagnosing radiative forcing and climate sensitivity, Geophysical Research Letters, 31, L03205, doi: 10.1029/2003GL018747.

Griffies, S. M., G. Danabasoglu, P. J. Durack, A. J. Adcroft, V. Balaji, C. W. Böning, E. P. Chassignet, E. Curchitser, J. Deshayes, H. Drange, B. Fox-Kemper, P. J. Gleckler, J. M. Gregory, H. Haak, R. W. Hallberg, P. Heimbach, H. T. Hewitt, D. M. Holland, T. Ilyina, J. H. Jungclaus, Y. Komuro, J. P. Krasting, W. G. Large, S. J. Marsland, S. Masina, T. J. McDougall,

A. J. G. Nurser, J. C. Orr, A. Pirani, F. Qiao, R. J. Stouffer, K. E. Taylor, A. M. Treguier, H. Tsujino, P. Uotila, M. Valdivieso, Q. Wang, M. Winton, and S. G. Yeager (2016): OMIP contribution to CMIP6: experimental and diagnostic protocol for the physical component of the Ocean Model Intercomparison Project. Geosci. Model Dev., 9, 3231–3296, https://doi.org/10.5194/gmd-9-3231-2016.

Grosfeld, K.; Treffeisen, R.; Asseng, J.; Bartsch, A.; Bräuer, B.; Fritzsch, B.; Gerdes, R.; Hendricks, S.; Hiller, W.; Heygster, G.; Krumpen, T.; Lemke, P.; Melsheimer, C.; Nicolaus, M.; Ricker, R. and Weigelt, M. (2016), Online sea-ice knowledge and data platform <www.meereisportal.de>, Polarforschung, Bremerhaven, Alfred Wegener Institute for Polar and Marine Research & German Society of Polar Research, 85 (2), 143-155, doi:10.2312/polfor.2016.011.

Haarsma RJ, Roberts MJ, Vidale PL, Senior CA, Bellucci A, Bao Q, Chang P, Corti S, Fuckar NS, Guemas V, von Hardenberg J, Hazeleger W, Kodama C, Koenigk T, Leung LR, Lu J, Luo J-J, Mao J, Mizielinski MS, Mizuta R, Nobre P, Satoh M, Scoccimarro E, Semmler T, Small J, von Storch J-S (2016) High Resolution Model Intercomparison Project (HighResMIP v1.0) for CMIP6. Geoscientific Model Development 9:4185-4208. https://doi.org/10.5194/gmd-9-4185-2016.

Hansen, J., R. Ruedy, M. Sato, and K. Lo, 2010: Global surface temperature change, Rev. Geophys., **48**, RG4004, doi:10.1029/2010RG000345.

Hausfather, Z. (2019): CMIP6: the next generation of climate models explained. Available online at https://www.carbonbrief.org/cmip6-the-next-generation-of-climate-models-explained (cited 20.12.2019).

Hegewald, J., 2019, seamore - cmorize simulation data to a given CMIP6 data request, doi:10.5281/zenodo.3585711.

Huffman, G. J., Adler R. F., Bolvin, D. T., and Gu, G. (2009) Improving the global precipitation record: GPCP version 2.1. Geophysical Research Letters 36(17):L17808.

IPCC, 2014: Climate Change 2014: Synthesis Report. Contribution of Working Groups I, II and III to the Fifth Assessment Report of the Intergovernmental Panel on Climate Change [Core Writing Team, R.K. Pachauri and L.A. Meyer (eds.)]. IPCC, Geneva, Switzerland, 151 pp.

Jung, T., M. J. Miller, T. N. Palmer, P. Towers, N. Wedi, D. Achuthavarier, J. M. Adams, E. L. Altshuler, B. A. Cash, J. L. Kinter III, L. Marx, C. Stan, and K. I. Hodges, 2012: High-resolution global climate simulations with the ECMWF model in Project Athena: Experimental design, model climate, and seasonal forecast skill. *J. Climate*, **25**, 3155–3172, doi:https://doi.org/10.1175/JCLI-D-11-00265.1

Kageyama, M., P. Braconnot, S. P. Harrison, A. M. Haywood, J. H. Jungclaus, B. L. Otto-Bliesner, J.-Y. Peterschmitt, A. Abe-Ouchi, S. Albani, P. J. Bartlein, C. Brierley, M. Crucifix, A. Dolan, L. Fernandez-Donado, H. Fischer, P. O. Hopcroft, R. F. Ivanovic, F. Lambert, D. J. Lunt, N. M. Mahowald, W. R. Peltier, S. J. Phipps, D. M. Roche, G. A. Schmidt, L. Tarasov, P. J. Valdes, Q. Zhang, and T. Zhou (2018): The PMIP4 contribution to CMIP6 - Part 1: Overview

and over-arching analysis plan. Geosci. Model Dev., 11, 1033–1057, https://doi.org/10.5194/gmd-11-1033-2018.

Kay, J. E., Holland, M. M., and Jahn, A. (2011): Inter-annual to multi-decadal Arctic sea ice trends in a warming world. Geophysical Research Letters, 38, L15708, doi: 10.1029/2011GL048008.

Knutti, R., Masson, D., and Gettelman, A. (2013), Climate model genealogy: Generation CMIP5 and how we got there, Geophys. Res. Lett., 40, 1194– 1199, doi:10.1002/grl.50256.

Korn, P. (2017) Formulation of an Unstructured Grid Model for Global Ocean Dynamics, Journal of Computational Physics 339, 525-552. doi.org/10.1016/j.jcp.2017.03.009.

Large WG, McWilliams JC, Doney SC (1994) Oceanic vertical mixing: a review and a model with a nonlocal boundary layer parameterization. Rev Geophys 32(4):363–403.

Lenderink, G., Buishand, A., and van Deursen, W. (2007) Estimates of future discharges of the river Rhine using two scenario methodologies: direct versus delta approach. Hydrol. Earth Syst. Sci., 11, 1145-1159.

Lenssen, N., G. Schmidt, J. Hansen, M. Menne,A. Persin,R. Ruedy, and D. Zyss, 2019: Improvements in the GISTEMP uncertainty model. J. Geophys. Res. Atmos., **124**, no. 12, 6307-6326, doi:10.1029/2018JD029522.

Loeb NG, Kato S, Su W, Wong T, Rose FG, Doelling DR, Norris JN, Huang X (2012) Advances in understanding top-of-atmosphere radiation variability from satellite observations. Surv Geophys 33:359-385.

Masson, D., and Knutti, R. (2011), Climate model genealogy, Geophys. Res. Lett., 38, L08703, doi:10.1029/2011GL046864.

McDonagh, E. L., King, B. A., Bryden, H. L., Courtois, P., Szuts, Z., Baringer, M., Cunningham, S. A., Atkinson, C., and McCarthy, G. (2015) Continuous estimate of Atlantic Oceanic freshwater flux at 26:5 N, J. Climate, 28, 8888-8906.

Mauritsen, T., et al. (2012), Tuning the climate of a global model, J. Adv. Model. Earth Syst., 4, M00A01, doi:10.1029/2012MS000154.

Meinshausen, M., Nicholls, Z., Lewis, J., Gidden, M. J., Vogel, E., Freund, M., Beyerle, U., Gessner, C., Nauels, A., Bauer, N., Canadell, J. G., Daniel, J., S., John, A., Krummel, P., Luderer, G., Meinshausen, N., Montzka, S. A., Rayner, P., Reimann, S., Smith, S. J., van den Berg, M., Velders, G. J. M., Vollmer, M., and Wang, H. J. (2019) The SSP greenhouse gas concentrations and their extensions to 2500. Geosci. Model Dev. Discuss., https://doi.org/10.5194/gmd-2019-222.

Meredith, M., Woodworth, P. L., Chereskin, T. K., Marshall, D. P., Allison, L. C., Bigg, G. R., Donohue, K., Heywood, K. J., Hughes, C. W., Hibbert, A., Hogg, A. M., Johnson, H. L., Jullion, L., King, B. A., Leach, H., Lenn, Y.-D., Morales-Maqueda, M. A., Munday, D. R., Naveira-

Garabato, A. C., Provost, C., Sallée, J.-B., and Sprintall, J. (2011) Sustained monitoring of the Southern Ocean at Drake Passage: past achievements and future priorities, Rev. Geophys., 49, L05603, doi:10.1029/2010RG000348.

Nature Communications editors (2019): A tug-of-war over the mid-latitudes. *Nat Commun* **10,** 5578, doi:10.1038/s41467-019-13714-0

Petersen, M. R., Asay- Davis, X. S., Berres, A. S., Chen, Q., Feige, N., Hoffman, M. J., et al. (2019). An evaluation of the ocean and sea ice climate of E3SM using MPAS and interannual CORE- II forcing. Journal of Advances in Modeling Earth Systems, 11, 1438– 1458. https://doi.org/10.1029/2018MS001373

Platnick S, King MD, Ackerman SA, Menzel WP, Baum BA, Riedi JC, Frey RA (2003) The MODIS cloud products: algorithms and examples from terra. IEEE Trans Geosci Remote Sens 41(2):459-473

Rackow, T, and Juricke, S. (2019) Flow- dependent stochastic coupling for climate models with high ocean- to- atmosphere resolution ratio. Q J R Meteorol Soc.; 1– 17. https://doi.org/10.1002/qj.3674

Rackow, T., Goessling, H. F., Jung, T., Sidorenko, D., Semmler, T., Barbi, D., & Handorf, D. (2018). Towards multi-resolution global climate modeling with ECHAM6-FESOM. Part II: climate variability. Climate Dynamics 50:2369, https://doi.org/10.1007/s00382-016-3192-6

Rackow T., Sein, D. V., Semmler, T., Danilov, S., Koldunov, N. V., Sidorenko, D., Wang, Y., Jung, T. (2019) Sensitivity of deep ocean biases to horizontal resolution in prototype CMIP6 simulations with AWI-CM1.0, Geosci. Model Dev., 12, 2635–2656, https://doi.org/10.5194/gmd-12-2635-2019

Rackow, T. , Sidorenko, D. , Goessling, H. F. , Timmermann, A. and Jung, T. (2014): Modeling ENSO with ECHAM6-FESOM: Influence of the ocean resolution, Ocean Sciences Meeting 2014, Hawaii Convention Center, Honolulu, USA, 23 February 2014 - 28 February 2014. https://doi.org/10.13140/2.1.2537.9209

Reichler T, Kim J (2008) How well do coupled models simulate today's climate? Bull Am Meteorol Soc 89(3):303–311

Ricker, R., Hendricks, S., Kaleschke, L., Tian-Kunze, X., King, J., & Haas, C. (2017). A weekly Arctic sea-ice thickness data record from merged CryoSat-2 and SMOS satellite data. The Cryosphere, 11, 1607–1623. https://doi.org/10.5194/tc-11-1607-2017

Ridderinkhof, H., van der Werf, P., Ullgren, J., van Aken, H., van Leeuwen, P., and de Ruijter, W. (2010) Seasonal and interannual variability in the Mozambique Channel from moored current observations, J. Geophys. Res., 115, C06010, doi:10.1029/2009JC005619.

Roach, A., Aagard, K., Pease, C., Salo, S., Weingartner, T., Pavlov, V., and Kulakov, M. (1995) Direct measurements of transport and water properties through Bering Strait, J. Geophys. Res., 100, 18443-18457.

Schauer, U., Beszczynska Moeller, A., Walczowski, W., Fahrbach, E., Piechura, J., and Hansen, E. (2008) Variation of measured heat flow through the Fram Strait between 1997 and 2006, in: Arctic-Subarctic Ocean Fluxes: Defining the Role of the Northern Seas in Climate, edited by: Dickson, R., Springer, 65-85.

Sein, D. V., Danilov, S., Biastoch, A., Durgadoo, J. V., Sidorenko, D., Harig, S., & Wang, Q. (2016). Designing variable ocean model resolution based on the observed ocean variability. Journal of Advances in Modeling Earth Systems, 8(2), 904-916.

Sein, D. V., Koldunov, N. V., Danilov, S., Wang, Q., Sidorenko, D., Fast, I., Rackow, T., Cabos, W. and Jung, T. (2017), Ocean Modeling on A Mesh with Resolution Following the Local Rossby Radius. Journal of Advances in Modeling Earth Systems, 9, 2601–2614. doi:10.1002/2017MS001099

Sein, D. V. , Koldunov, N. V., Danilov, S., Sidorenko, D., Wekerle, C., Cabos, W., Rackow, T., Scholz, P., Semmler, T., Wang, Q. and Jung, T. (2018). The Relative Influence of Atmospheric and Oceanic Model Resolution on the Circulation of the North Atlantic Ocean in a Coupled Climate Model. Journal of Advances in Modeling Earth Systems. doi:10.1029/2018MS001327

Semmler, Tido; Danilov, Sergey; Rackow, Thomas; Sidorenko, Dmitry; Hegewald, Jan; Sein, Dmitri; Wang, Qiang; Jung, Thomas (2017). AWI AWI-CM 1.1 HR model output prepared for CMIP6 HighResMIP. Earth System Grid Federation. http://cera-www.dkrz.de/WDCC/meta/CMIP6/CMIP6.HighResMIP.AWI.AWI-CM-1-1-HR

Semmler, Tido; Danilov, Sergey; Rackow, Thomas; Sidorenko, Dmitry; Barbi, Dirk; Hegewald, Jan; Sein, Dmitri; Wang, Qiang; Jung, Thomas (2018). AWI AWI-CM1.1MR model output prepared for CMIP6 CMIP. Version 20191219. Earth System Grid Federation. https://doi.org/10.22033/ESGF/CMIP6.359

Semmler, Tido; Manzini, Elisa; Matei, Daniela; Pradhan, Himansu Kesari; Jung, Thomas (2019). AWI AWI-CM1.1MR model output prepared for CMIP6 PAMIP pdSST-pdSIC. Version 20191219.Earth System Grid Federation. https://doi.org/10.22033/ESGF/CMIP6.12040

Sidorenko, D., Rackow, T., Jung, T., Semmler, T., Barbi ,D., Danilov, S., Dethloff ,K., Dorn, W., Fieg, K., Goessling, H. F., Handorf, D., Harig, S., Hiller, W., Juricke, S., Losch, M., Schröter, J., Sein, D. V., Wang, Q., (2015). Towards multi-resolution global climate modeling with ECHAM6–FESOM. Part I: model formulation and mean climate. Climate Dynamics, 44(3-4), 757-780.

Smedsrud, L. H., Ingvaldsen, R., Nilsen, J. E. Ø., and Skagseth, Ø. (2010) Heat in the Barents Sea: transport, storage, and surface fluxes, Ocean Sci., 6, 219-234.

Smith DM, Screen JA, Deser C, Cohen J, Fyfe JC, Garcia-Serrano J, Jung T, Kattsov V, Matei D, Msadek R, Peings Y, Sigmond M, Ukita J, Yoon J-H, Zhang X (2018) The Polar Amplification Model Intercomparison Project (PAMIP) contribution to CMIP6: investigating the causes and consequences of polar amplification. Geoscientific Model Development Discussions. https://doi.org/10.5194/gmd-2018-82

Steele, M., Morley, R., and Ermold, W. (2001): PHC: A Global Ocean hydrography with a high-quality Arctic Ocean, Journal of Climate, 14, 2079-2087.

Stevens B, Giorgetta M, Esch M, Mauritsen T, Crueger T, Rast S, Salzmann M, Schmidt H, Bader J, Block K, Brokopf R, Fast I, Kinne S, Kornblueh L, Lohmann U, Pincus R, Reichler T, Roeckner E (2013) Atmospheric component of the MPI-M earth system model: ECHAM6. J Adv Model Earth Syst 5(2):146–172

Stocker, Thomas, ed. *Climate change 2013: the physical science basis: Working Group I contribution to the Fifth assessment report of the Intergovernmental Panel on Climate Change*. Cambridge University Press, 2014.

Stroeve, Julienne, and Dirk Notz. "Insights on past and future sea-ice evolution from combining observations and models." *Global and Planetary Change* 135 (2015): 119-132.

Tonboe, R. T., Eastwood, S., Lavergne, T., Sørensen, A. M., Rathmann, N., Dybkjær, G., Pedersen, L. T., Høyer, J. L., and Kern, S. (2016): The EUMETSAT sea ice concentration climate data record, The Cryosphere, 10, 2275–2290, https://doi.org/10.5194/tc-10-2275-2016

Turner, John, et al. "Recent changes in Antarctic sea ice." *Philosophical Transactions of the Royal Society A: Mathematical, Physical and Engineering Sciences* 373.2045 (2015): 20140163.

Wang Q, Danilov S, Sidorenko D, Timmermann R, Wekerle C, Wang X, Jung T, Schröter J (2014) The Finite Element Sea Ice-Ocean Model (FESOM) v.1.4: formulation of an ocean general circulation model. Geosci Model Dev 7:663–693

Wang, C., Zhang, L., Lee, S.K., Wu, L. and Mechoso, C.R., 2014. A global perspective on CMIP5 climate model biases. Nature Climate Change, 4(3), p.201.

Wang, Q., Wekerle, C., Danilov, S., Wang, X. and Jung, T. (2018). A 4.5 km resolution Arctic Ocean simulation with the global multi-resolution model FESOM 1.4, Geosci. Model Dev., 11, 1229-1255.

Weaver, A. J., Sedláček, J., Eby, M., Alexander, K., Crespin, E., Fichefet, T., Philippon-Berthier, G., Joos, F., Kawamiya, M., Matsumoto, K., Steinacher, M., Tachiiri, K., Tokos, K., Yoshimori, M., Zickfeld, K. (2012) Stability of the Atlantic meridional overturning circulation: A model intercomparison. *Geophys. Res. Lett.* **39**, L20709.

Weijer, W., Cheng, W., Drijfhout, S. S., Fedorov, A. V., Hu, A. V., Jackson, L. C., Liu, W., McDonagh, E. L., Mecking, J. V., & Zhang, J. (2019). Stability of the Atlantic Meridional Overturning Circulation: A Review and Synthesis. Journal of Geophysical Research: Oceans. https://doi.org/10.1029/2019JC015083

Wekerle, C., Q. Wang, S. Danilov, T. Jung, and J. Schröter (2013), The Canadian Arctic Archipelago throughflow in a multiresolution global model: Model assessment and the driving mechanism of interannual variability, J. Geophys. Res. Oceans, 118, 4525–4541, doi:10.1002/jgrc.20330.

Woodgate, R. A., 2018. Increases in the Pacific inflow to the Arctic from 1990 to 2015, and insights into seasonal trends and driving mechanisms from year-round Bering Strait mooring data. *Progress in Oceanography*, 160: 124-154.

Zampieri, L., and Goessling, H. F. (2019). Sea ice targeted geoengineering can delay Arctic sea ice decline but not global warming. Earth's Future. 7. https://doi.org/10.1029/2019EF001230

Zappa, G., Shaffrey, L. C. and Hodges, K. I. (2013) The ability of CMIP5 models to simulate North Atlantic extratropical cyclones. Journal of Climate, 26, 5379--5396, doi: https://doi.org/10.1175/JCLI-D-12-00501.1

Zappa, G., and Shepherd, T. G. (2017): Storylines of Atmospheric Circulation Change for European Regional Climate Impact Assessment. Journal of Climate, 30, 6561-6577, doi: https://doi.org/10.1175/JCLI-D-16-0807.1